FUEL REGRESSION CHARACTERISTICS IN STABILIZED COMBUSTION WITH LIQUID OXYGEN

Ayumu TSUJI

LIST OF CONTENTS

LIST OF FIGURES

LIST OF TABLES

CHAPTER 1.

INTRODUCTION

1.1. Axial-Injection End-Burning Hybrid Rockets

The artificial satellite market has continued to expand in recent years. Market analysts expect the scale to double within the next ten years [1]. While the number of large satellites launched has remained constant, the number of small and microsatellite launches of 50 kg or less has increased dramatically [2]. Nowadays, the orbit insertion of small and microsatellites is primarily carried out via piggybacking, which refers to the use of surplus space surrounding the primary satellite in large rocket launches for delivering clusters of small satellites. The releasing of these small satellites can also be carried out from the ISS (International Space Station). Since it is difficult to put satellites into suitable orbits for the mission at hand when piggybacking, share-riding, and ISS release, the demand for small launchers which can deliver small satellites to selective orbits keeps increasing. The need for low-cost and small-scale rockets is urgent, because the small rockets currently in operation are still expensive, and there are few launch opportunities [3].

Hybrid rockets attract attention as an attractive rocket because it is superior in safety and can significantly reduce launch costs. This is because hybrid rockets generally use a liquid phase oxidizer and a solid phase hydrocarbon polymer compound as fuel. However, despite years of research, only Scaled Composites' Space Ship One has successfully yielded practical use, and it itself cannot place a payload into orbit. Low thrust and oxidizer to fuel ratio shifting (O/F shifting) during firing and throttling operation, which decrease performance, are the main reasons why hybrid rockets have not been put into practical use [4]. It is necessary to improve the fuel regression rate so that hybrid rockets can generate thrust enough to reach an orbit. Such methods as imposing a vigorous swirl to the oxidizer flow supplied to the combustion chamber or using low melting point fuels are still under development. However, no research had reported fuel regression rates that exceed the burning rate of composite solid propellants; e.g., the burning rate of SRB-A, which is a solid rocket booster of H-IIA rockets, is around 10 mm/s under operational chamber pressure of 10 MPa, but that of conventional hybrid

rockets is less than1.0 mm/s [5,6].

Nagata et al. proposed the concept of axial-injection end-burning hybrid rockets (AIEB) shown in Fig 1.1, which employ a cylindrical fuel having numerous ports in the fuel axis direction and only burns at the downstream end surface [7–10]. An AIEB hybrid rocket employs stabilized combustion, which results when an oxidizer flows through submillimeter order ports at a velocity such that a diffusion flame maintained at the port exit does not propagate upstream – i.e., into the port. Stabilized combustion sustained at every small port forms an aggregate of minute diffusion flames, and the rear-end surface regresses in the upstream direction with a constant burning area. Saito et al. have revealed that the fuel regression rate is proportional to chamber pressure, and that O/F remains constant during firing [11,12]. Furthermore, Okutani et al. experimentally confirmed that the fuel regression rate exceeds 10 mm/s at a chamber pressure of around 1 MPa when using gaseous oxygen as the oxidizer, and suggested that it is possible to overcome the disadvantages of low thrust under higher pressure conditions [13]. The regression rate reported in these investigations exceeds that of solid rockets and conventional hybrid rockets. Saito et al. also revealed that O/F shifting did not occur in a throttling operation during firing tests [14]. These investigations prove that AIEB hybrid rockets may overcome all the biggest problems that have hindered the realization of conventional hybrid rockets, and can be put into practical use as launch vehicle propulsion systems.

In recent years, Hitt et al. and Okuda et al. have researched supplying gaseous nitrous oxide as a storable oxidizer. They have shown the achievement of end burning similar to gaseous oxygen, whose results develop the other use of AIEB hybrid rockets for the thruster on spacecraft [15,16].

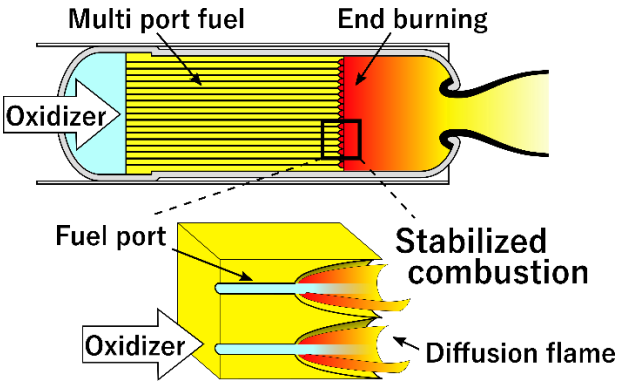

Fig.1.1 Schematic drawing of axial-injection end-burning hybrid rockets.

1.2. Flame Spreading into a Solid Fuel Duct

The combustion of AIEB hybrid rocket is an aggregation of minute diffusion flames sustained at each small port exit. Previous experimental studies by Saito et al. have revealed that single-port fuels and multi-port fuels employed under the AIEB hybrid rockets configuration have the same combustion characteristics [12] [10]. Therefore, the study of flame spreading into single-port fuel is enough to understand the essential combustion characteristics of AIEB hybrid rockets. Hashimoto et al. and Matsuoka et al. studied the flame spreading into single-port fuels using gaseous oxygen. Hashimoto et al. found a new combustion mode that the diffusion flame could not enter into a virgin port and sustained behind the tip of an enlarged port when the oxidizer port velocity exceeds a certain level [17]. Beyond this velocity, the flame spread rate coincides with the axial fuel regression rate. Thus, the flame is maintained at the port exit, and expands the port exit region into a bell-shape. They named this new combustion mode stabilized combustion. Stabilized combustion flames sustained at the exit of an array of numerous small ports results in the end-burning mode of AIEB hybrid rockets. Hashimoto et al. also reported that the axial fuel regression rate of stabilized combustion using gaseous oxygen decreases with increasing oxidizer port velocity and proportionally increases with increasing ambient pressure. They reported no apparent effect of a port diameter on the axial fuel regression rate and proposed the following empirical formula of the axial fuel regression rate;

$$V_f = \left(\frac{C_1}{V_{ox}} + C_2\right) {P_c}^n \qquad (1.1)$$

V_{ox} is the oxidizer port velocity, P_c is the ambient pressure, and C_1, C_2, and n are empirical constants. In particular, n is called the pressure exponent, and they reported n=0.951, which was close to unity. When the unit of each parameter is [m/s] for V_f and V_{ox} and [Pa] for P_c, they also showed the remaining empirical constants were C_1=1.34×10^{-7}, C_2=1.61×10^{-9}.

In addition to investigating the axial fuel regression characteristics of stabilized combustion, they also experimentally investigated the conditions which sustain stabilized combustion. When oxidizer port velocity is below a certain level, diffusion flame spreads into the port at high speed. This combustion mode is called flame-spreading combustion to distinguish it from stabilized combustion. Because spreading combustion mode causes backfiring in AIEB hybrid rockets, it is necessary to prevent the mode from occurring. Hashimoto et al. focused on momentum transport from the mainstream to the vicinity of an inner port wall surface. They showed that the friction velocity on the

inner port wall surface could explain the transition from flame spreading mode to stabilized combustion mode [18]. Matsuoka et al. proposed a theory of the transition between two combustion modes according to the Damkohler number. They concluded that when the oxidizer port velocity reaches blow-off condition, the tip of an enlarged duct sustains the diffusion flame without blowing off, and the combustion mode becomes stabilized combustion [19]. In this way, Hashimoto and Matsuoka et al. have studied the physical mechanism of the transition between stabilized combustion and flame-spreading combustion. Still, the axial fuel regression rate of stabilized combustion is limited to experimental research, and there has not been any research working on the construction of a physical model.

1.3. Model of Opposed Flow Flame Spreading over a Solid Fuel

Although there is a difference in the flame spread rate between flame-spreading combustion and stabilized combustion, the principal mechanism should be that the diffusion flame moves upstream while heating and decomposing - i.e., regressing - the surrounding fuel surface in the same manner. Many studies to date have proposed models for flame spread rate over a solid fuel surface [20,21]. Focusing on the heat energy balance between the fuel and diffusion flame, Williams and Pello et al. showed that the thermal feedback from a diffusion flame to an unburned fuel surface dominated the flame-spread rate [22,23]. Although there are multiple heat transfer paths to unburned fuel, Ito et al. optically observed the temperature distribution inside a solid fuel using a holographic interferometer and investigated the dominant heat transfer path from the calculated heat flux [24]. The result revealed that the gas-phase heat conduction from a diffusion flame to a fuel surface is dominant in the flame spread rate over a parallel flat fuel plate. They also reported that heat conduction in the upstream direction in a solid fuel becomes dominant near the blow-off limit, and around 13% of the input heat to unburnt fuel was released from the fuel surface [25]. They modeled an opposed flow flame spread rate from the obtained energy balances and reported that the spread rate is proportional to the net heat flux input to the unburned fuel. Because flame-spreading combustion around the blow-off limit is also close to the transition to stabilized combustion, their research's results infer that the net heat input to the unburned fuel also determines the axial fuel regression rate of stabilized combustion. The granular diffusion flame (GDF) model is one method for estimating the amount of heat input to solid fuel from flame [26]. The GDF model is a regression model of a solid propellant in which fuel and oxidizer are mixed in advance. Since the model calculates the distance between the flame and the propellant surface, taking the diffusion and chemical kinetics of vaporized oxidizer and fuel into account, increasing

pressure reduces the chemical reaction time, leading the flame to approach the fuel surface and resulting in increasing the heat flux to the fuel. Applying the GDF model, Saito and Hitt et al. constructed a fuel regression model for an AIEB hybrid rocket by estimating the amount of heat input from a diffusion flame to a fuel surface. Their models can also explain the pressure dependence of the regression rate [27,28].

1.4. Flame Spreading in a Solid Fuel Duct with Liquid Oxidizer

Though, as previously stated, almost all the studies on the flame spreading in solid fuel duct have supplied gaseous oxidizers such as air, oxygen, or nitrous oxide, there are also a few studies using a liquid oxidizer. Yuasa et al. proposed a gas generator utilizing solid combustion for swirl flow hybrid rockets and investigated the combustion characteristics by directly supplying liquid oxygen to solid fuel [29]. As a preliminary experiment, they burned a rod of polymethyl methacrylate (PMMA) in liquid oxygen under 5 MPa of ambient pressure, which reported that, despite unstable combustion, the flame spread rate was around 3 mm/s. Tomizawa et al. used cylindrical PMMA fuel which has multiple ports in the axial direction as a gas generator fuel, and installed it upstream of a swirl flow injector to conduct a demonstration firing test [30]. They found that fuel's entire inner port surfaces did not burn and a bell-shaped fuel regression shape formed at port exit similar to stabilized combustion. Following the AIEB hybrid rocket proposed by Nagata et al., Takei et al. proposed the AIEB type gas generator utilizing this combustion mode and constructed an empirical formula for axial fuel regression rate at a port diameter of 3.0 mm as the following Eq. 1.2 [31].

$$V_f = 0.043 V_{ox} + 0.28 \qquad (1.2)$$

V_f [mm/s] is axial fuel regression rate and V_{ox} [m/s] is oxidizer port velocity. However, in their results, there are several uncertain points and unreasonable assumptions. Because they designed the experimental setup as a gas generator, which supplied atomized liquid oxygen to each fuel port, the measured oxidizer port velocity must have been incorrect. Also, since it was impossible to directly observe the combustion state of the solid fuel stored inside the combustor, they constructed the empirical formula using fuel mass consumption measured after firing. Therefore, this formula is unreliable. In conclusion, the characteristics of flame spreading in a solid fuel duct with a liquid oxidizer remains unclear.

1.5. Research Purpose

The AIEB hybrid rocket concept is attractive for use as a launch vehicle propulsion system due to the high fuel regression rates (of over 10 mm/s) and no-O/F shifting. However, all the firing tests performed in previous studies have used only gaseous oxidizers, which are impractical for use in launch vehicles. Gaseous oxidizers require large-capacity and/or heavy oxidizer tanks that can withstand high internal pressure. As with existing liquid rockets, launch vehicles need to load and store an oxidizer as a liquid phase because a liquid phase density is much higher than that of a gaseous phase. To supply an oxidizer to the fuel in a gaseous phase requires a gas generator or a regenerative cooling device to gasify a liquid oxidizer, which leads to a complicated structure and an increase in cost. Since small satellite launchers are required to be inexpensive, it is preferred to eliminate these gasifying devices and directly supply an oxidizer to the fuel in a liquid phase. However, the fuel regression and the flame spreading characteristics in a solid fuel duct with a liquid oxidizer remain unclear. The studies by Takei et al. cannot explain in enough detail these characteristics. The present research is the first experimental study on the fuel regression characteristics of flame spreading in a solid fuel duct with liquid oxygen, in which a model for fuel regression rate is proposed and verified through firing tests.

1.6. Structure of the Thesis

The structure of this thesis is as follows:

Chapter 1 is an introduction that explains the background and purpose of this research.

Chapter 2 explains the experimental setup, procedures, and data reduction method.

Chapter 3 presents an overview of flame spreading in a solid fuel duct with liquid oxygen as observed in firing tests, and reports extinction and abnormal regression.

Chapter 4 addresses the effect of port diameter, oxidizer port velocity, and chamber pressure on axial fuel regression rate and the construction of an empirical formula.

Chapter 5 explains the derivation of the model for the axial fuel regression rate considering a heat energy balance in the solid fuel, and discusses its validity through comparison to the experimental

results. This chapter also reveals the influence of each physical mechanism/parameter of the model: port diameter, oxidizer port velocity, and chamber pressure.

Chapter 6 addresses the effects of port diameter, oxidizer port velocity, and chamber pressure on a fuel regression shape and construction of an empirical formula. Besides, the calculated results are shown, which estimate the amount of un-vaporized liquid oxygen exhausted from a port without combustion utilizing the constructed model.

Chapter 7 is the concluding remarks.

CHAPTER 2.

EXPERIMENTAL SETUP AND DATA REDUCTION

The flame of stabilized combustion is a diffusion flame sustained at the fuel port exit through which an oxidizer flows, and the end-burning in an AIEB hybrid rocket consists of the aggregation of these diffusion flames. Therefore, the principal combustion characteristics of an AIEB hybrid rocket are the same as the stabilized combustion sustained at the exit of single port fuel. The principal combustion and fuel regression characteristics of the stabilized combustion sustained in a PMMA single-port fuel acquired by Hashimoto et al. are consistent with that in a multi-port fuel manufactured by a stereolithography 3D printer acquired by Saito et al. [7,10]. This research is an investigation of the principal fuel regression characteristics of AIEB hybrid rockets when oxidizer is supplied to the fuel ports in the liquid phase. Experiments were conducted in the same manner as Hashimoto's study, using experiments with single port fuels to collect data relevant to the modeling of AIEB hybrid rockets fuel regression rate. Liquid oxygen was used as an oxidizer because the combustion characteristics with its gas-phase have been well investigated.

2.1. Fuel Sample

Since it was necessary to measure the fuel regression rate as a principal fuel regression characteristic, prismatic blocks of PMMA, which allowed for the observation of the internal port state during combustion, were used as fuels. Figure 2.1 is a schematic of one of the fuels employed. Experiments employed a rectangular block with a width of 30 mm, a height of 70 mm, and a depth of 20 mm instead of a circular pipe because the flat surface does not refract and distort the internal port's image. The fuel had a single port in the longitudinal direction at the center through which liquid oxygen flows, and a female taper screw of Rc 1/8 inch on the port upstream to connect with the liquid oxygen supply tube whose diameter was 1/4 inch. An expansion part of the port exit had an ignition apparatus ignite the port exit edge's entire circumference so that the fuel could regress uniformly without bias. The port length excluding the inlet was 50 mm, which was too short for the boundary layer of liquid oxygen flowing inside to fully develop, but long enough to prevent liquid oxygen from boiling due to

external heat input. Fuel port sizes varied from 1.0, 2.0, 3.0 and 6.0 mm in diameter. All fuel grains except for the 6.0 mm port diameter were prepared in-house by drilling a cylindrical port. On the fuels which had port diameters of 6.0 mm were manufactured from an extruded pipe with an outer diameter of 12 mm to ensure port diameter accuracy, because large ports manufactured by drilling do not have less than 1 mm variation due to sticky chips getting entangled in a drill. Figure 2.2 shows the outer view of a fuel sample with an ignition apparatus. An acrylic adhesive glue was used to affix the ignition apparatus to the end of the fuel. The ignition apparatus consists of a nichrome wire as a heating element, and Scotch Brite™ as an accelerant to the fuel rear end face. The nichrome wire is heated using an AC power source, which causes deflagration of the accelerant, such that when oxidizer is supplied to the fuel port a diffusion flame forms at the port exit.

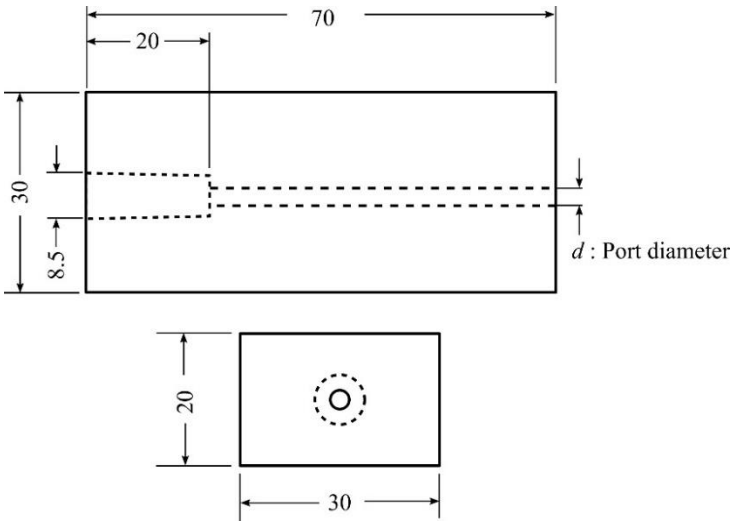

Fig.2.1 Schematic of PMMA fuel.

Fig.2.2 Picture of a fuel sample with ignition apparatus.

2.2. Experimental Apparatus

Figure 2.3 is a schematic of the experimental apparatus. The experimental apparatus mainly consists of a combustion part, a feeding part, and a measurement part. The feeding part mainly consisted of a liquid oxygen feed line, a cooling line using liquid nitrogen, and two gaseous nitrogen lines; one was for stopping the combustion, and the other was for pressurizing the combustion chamber. A reservoir insulated with urethane foam was used to store liquid oxygen, and a vacuum pump was connected to the reservoir for cooling by decompressing and vaporizing liquid oxygen. Also, a pressurization line for pressurizing the reservoir and a liquid oxygen feed line are connected to the

reservoir. Helium gas, whose solubility in liquid oxygen is low, pressurized the reservoir to feed liquid oxygen to the fuel sample. In feeding liquid oxygen, three measures were taken to prevent liquid oxygen from being a two-phase flow. The first measure taken was depressurization of the reservoir inside by the vacuum pump. The latent heat of vaporization induced by depressurization decreased liquid oxygen temperature to below the boiling point in atmospheric pressure. The second measure taken was the use of liquid nitrogen as a coolant for the oxidizer feed line. The oxidizer feed line passed through a larger-diameter concentric liquid nitrogen coolant line so that the feed line was cooled to the same temperature as liquid nitrogen boiling point under atmospheric pressure. Liquid nitrogen was supplied from a vacuum insulated vessel to the concentric tubing annulus through a siphon pressurized by gaseous nitrogen, and was discharged to the atmosphere after cooing. The third measure taken was the installation of the pressurizing line orifice inside of the liquid oxygen reservoir to reduce the tubing surface area exposed to heat input from the outside. The nitrogen gas lines for stopping combustion and pressurizing the combustion chamber were branched from the same nitrogen gas cylinder and connected to the liquid oxygen feed line and the combustion chamber, respectively. During firing, nitrogen gas heated by an electric heater was supplied only into the combustion chamber. After that, a ball valve switched the flow path to the liquid oxygen feed line to stop combustion.

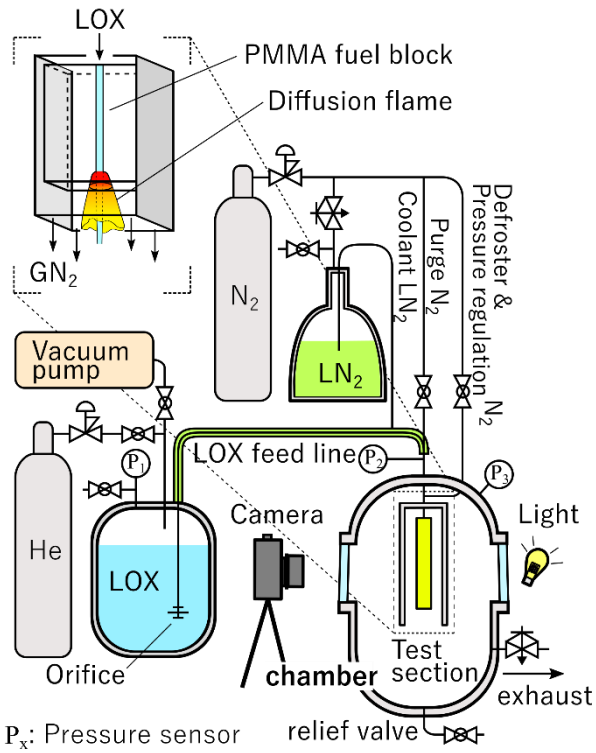

Fig.2.3 Schematic of the experimental apparatus.

The combustion part consisted of a combustion chamber, a combustion duct, and a container to receive and contain liquid oxygen. The combustion state of a fuel sample inside the combustion chamber with small windows was observed while regulating chamber pressure. Figure 2.4 show pictures of the combustion duct with a fuel sample installed. The combustion duct was rectangular, such that two sides of it consisted of PMMA flat plates to observe a fuel sample installed inside the duct, and installed in the combustion chamber so that the port is in the vertical direction. Liquid oxygen was supplied into a port from the upper side of fuel so that a flame spread to the upstream direction. This was because liquid oxygen discharged from the port flowed downward by gravity to prevent the fuel surface and the combustion duct from burning. The liquid oxygen discharged from the port exit was received and stored in the container connected to the combustion chamber. The container was also cooled with liquid nitrogen so that the vaporized liquid oxygen did not raise chamber pressure. Heated nitrogen gas passing through the combustion duct between the fuel surfaces and PMMA flat plates prevented the fuel surface from being roasted by uplifted flame and frosted due to liquid oxygen cooling. The heated nitrogen gas also pressurized the combustion chamber to a predetermined pressure. The gas inside the chamber was released to the atmosphere through a manually controlled needle valve or back pressure regulator to keep chamber pressure constant.

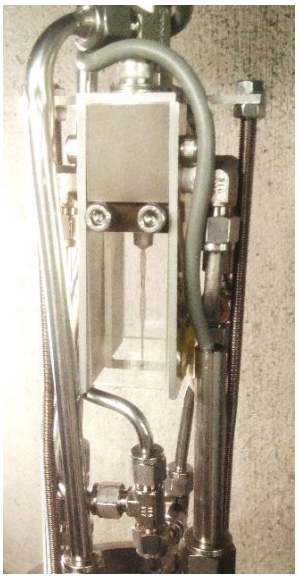

(a) Overview of the combustion duct.

(b) Inside of the duct with a fuel sample installed.

Fig.2.4 Pictures of the combustion duct and a fuel.

The measurement part consisted of optical observation with a video camera, chamber pressure measurement, and liquid oxygen flow rate measurement. A video camera filmed the combustion state from the one window, while a LED backlight was used to illuminate the flame tip position from the other window. The flame tip position was used to determine the axial fuel regression rate. A pressure transducer was used to measure the chamber pressure. The oxidizer mass flow rate of liquid oxygen was calculated from the pressure drop across the orifice, as measured using two pressure transducers. In this case, the reservoir pressure was used as the orifice upstream pressure, and the static pressure in the fuel upstream feed line was used as the orifice downstream pressure.

2.3. Experimental Procedure

Filling liquid oxygen into the reservoir, set the video camera, and helium gas pressure conducted before starting the experimental sequence. An experiment takes the following procedure (see below). After completing the procedure, stop data recording and helium gas pressurization and release the reservoir pressure after confirming safety. Finally, remove a fuel sample from the combustion duct.

(1) Turn on the vacuum pump and start depressurizing the reservoir filled with liquid oxygen.
(2) Start supplying liquid nitrogen to cool the liquid oxygen feed line and the container of liquid oxygen connected to the combustion chamber.
(3) Confirm that the reservoir pressure dropped to 0.03 MPa or less, and that liquid nitrogen begins to flow out from the cooling line to the atmosphere.
(4) Turn on the heater's power and supply nitrogen gas to the line for pressurizing the combustion chamber, which fills the combustion chamber with nitrogen gas through the combustion duct.
(5) Operate the manual needle valve or back pressure regulator of the chamber pressure to regulate the chamber pressure.
(6) Start all data acquisition.
(7) After closing the line from the reservoir to the vacuum pump, pressurize the reservoir with helium gas and open the liquid oxygen supply line's valve to start supplying liquid oxygen to the fuel.
(8) Confirming that the liquid oxygen supplied to the fuel changes from two-phase flow to liquid phase flow. Then, energize the nichrome wire to ignite the fuel.
(9) After confirming that the flame spreads upstream to around 80% of the total length of the port, close the liquid oxygen supply line, supply nitrogen gas into the fuel port to stop combustion by switching the valve from the chamber pressurization line to the liquid oxygen feed line. Simultaneously, open the large-diameter exhaust valve attached to the chamber to reduce the

chamber pressure, rapidly extinguishing the flame.

2.4. Data Reduction Method

2.4.1. Calculation of Oxidizer Port Velocity

Though the fuel port diameter and the chamber pressure can be measured directly with a pin gauge or a pressure transducer, the oxidizer port velocity and mass flow rate of liquid oxygen were calculated from the pressure drop across an orifice measured by two pressure transducers. The following equations give the oxidizer port velocity, V_{ox}, and the mass flow rate of liquid oxygen, $\dot{m}_{ox}$.

$$V_{ox} = \frac{4\overline{\dot{m}_{ox}}}{\pi \rho_{ox} d^2} \quad (2.1)$$

$$\dot{m}_{ox} = \frac{C(Re_D)}{\sqrt{1-\beta^4}} A_o \sqrt{2\rho_{ox}(P_1 - P_2)} \quad (2.2)$$

$\overline{\dot{m}_{ox}}$ is the time-averaged oxidizer mass flow rate, d is the port diameter, β is the diameter ratio of an orifice, A_o is the orifice diameter, ρ_{ox} is the liquid oxygen density, P_1 is the reservoir pressure, and P_2 is the static pressure of the feed line upstream on fuel. The orifice diameter, d_o, and the pipe diameter of the pipe attached to an orifice, D, define the orifice diameter ratio, β, as the following; $\beta = (d_o/D)^2$. The calculation uses the density of liquid oxygen of 1190 kg/m^3 in the boiling point of liquid nitrogen under atmospheric pressure of 80 K. According to an experimental condition. The feed system selected an appropriate orifice diameter according to an experimental condition from 0.5, 1.0, and 1.7 mm. Since this calculation method cannot apply to a two-phase flow, the analysis did not use the data when the supplied liquid oxygen was a two-phase flow. When the Reynolds number, Re_D, whose representative length is the pipe diameter, D, exceeds 10^4, the discharge coefficient, C, is constant regardless of the Reynolds number. However, below 10^4, the coefficient changes greatly depending on the Reynolds number [32]. For some experiments, in which the Reynolds number decreased below 10^4, the calculation used a discharged coefficient as a function of Reynolds number, Re_D, which was obtained from water flow tests for each orifice to investigate the relation between the coefficient and the Reynolds number. According to Eq. 2.2, Reynolds number is necessary to calculate the mass flow rate, $\dot{m}_{ox}$, from the discharge coefficient, $C(Re_D)$. However, Reynolds number is unknown without calculating the oxidizer mass flow rate from the discharge coefficient. Therefore, iterative calculations are necessary to acquire oxidizer mass flow rate.

2.4.2. Calculation of Axial Fuel Regression Rate

The calculation of the axial fuel regression rate uses the data ($x_{f,i}$, t_i) acquired from the video captured by the camera, where t is time, and x_f is the flame tip position. Using the time history of the flame tip position when the moving velocity was constant, the least-squares method calculates the axial fuel regression rate, V_f, as a slope of the regression line shown in Eq. 2.3 from Eq. 2.2.

$$x_f = V_f t \quad (2.3)$$

$$V_f = \frac{\sum(t_i - \bar{t})(x_{f,i} - \overline{x_f})}{\sum(t_i - \bar{t})^2} \quad (2.4)$$

The standard error, δ_{V_f}, of the regression coefficient is used as the measurement error of the axial fuel regression rate. δ_{V_f}means that the 68% confidence interval of the axial fuel regression rate is $\pm\delta_{V_f}$. From the definition of standard error, δ_{V_f} is calculated by Eq. 2.2, where n is the number of sample data.

$$\delta_{V_f} = \sqrt{\frac{\sum(x_{f,i} - V_f t_i)^2}{(n-2)\sum(t_i - \bar{t})^2}} \quad (2.5)$$

2.4.3. Error Analysis

Based on the law of error propagation, the error of the oxidizer flow velocity, $\delta_{V_{ox}}$, is calculated from Eq. 2.2, where δ_{P_1} is the error bias of the pressure transducer that measures the reservoir pressure and δ_{P_2} is the error bias of the pressure sensor that measures the feed line pressure.

$$\delta_{V_{ox}} = \sqrt{\left(\frac{\partial V_{ox}}{\partial P_1}\right)^2 {\delta P_1}^2 + \left(\frac{\partial V_{ox}}{\partial P_2}\right)^2 {\delta P_2}^2} \quad (2.6)$$

The pressure transducer's error bias is used as the chamber pressure error except for an experiment when the pressure fluctuated wildly during firing. In this case, the standard deviation of the acquired pressure history corresponds to the chamber pressure error. When the oxidizer port velocity fluctuated widely during firing, the error was the larger one of the standard deviation or the error calculated from Eq. 2.2.

CHAPTER 3.

FUEL REGRESSION AND COMBUSTION BEHAVIOR

The present research is the first experimental study on the fuel regression characteristics of flame spreading in a solid fuel duct with completely liquid phase oxygen. This chapter briefly explains the combustion behavior with liquid oxygen, such as burning velocity and combustion modes. The author discusses the combustion modes: stabilized combustion, abnormal regression, and extinction observed in experiments, comparing with previous researches studying the flame spreading with gaseous oxygen. The author also indicates a strong cooling effect by liquid oxygen, referring to the temperature distribution difference at the tip of an enlarged fuel duct between gaseous oxygen and liquid oxygen case.

3.1. Classification of the Combustion Mode

The author studied the flame spreading into a fuel duct with liquid oxygen under atmospheric pressure and investigated the effect of port diameter and oxidizer port velocity on axial fuel regression rate [33]. Figure 3.1 shows the combustion state of a solid fuel duct with liquid oxygen under atmospheric pressure when the port diameter was 1.0, 2.0, 3.0, and 6.0 mm. These pictures show that most of the liquid oxygen supplied to the fuel exit from the port exit without vaporizing, which suggests that liquid oxygen passed through the center of the cylindrical diffusion flame formed along the regressing fuel surface. The fuel regression shape was like a bell-shape, and the diffusion flame appeared behind the tip of the enlarged port, moving upstream slowly. Since the diffusion flame moved with duct's expanded section without propagating into the duct, it can be said that the flame spread rate is equivalent to the axial fuel regression rate. In the experiments, the regression rate was relatively slow, around 0.2 to 0.5 mm/s under atmospheric pressure. Previous studies investigating the flame spreading into a solid fuel duct with gaseous oxygen reported that the regression rate under the atmospheric pressure was around 0.5 to 1 mm/s in stabilized combustion and around 5 to 10 mm/s in flame-spreading combustion [7,16]. Compared with these studies, the flame spread rate with liquid oxygen was around 1/20 of the rate in flame-spreading combustion and around half in stabilized

combustion with gaseous oxygen. Though the flame spread rate with liquid oxygen was slower than in both cases, the rate was relatively closer to that of stabilized combustion.

The following three points summarize the characteristics of fuel regression and combustion behavior of flame spreading in a solid fuel duct as with liquid oxygen.

(1) The fuel port exit regresses into a “bell-shape”.
(2) The moving velocity of the tip of the enlarged fuel duct (i.e., the axial fuel regression rate) is equivalent to the flame spread rate.
(3) The flame spread rate is slow, less than 1 mm/s under atmospheric pressure.

These three characteristics are consistent with stabilized combustion under gaseous oxygen, which means that the flame spreading under liquid oxygen can be classified as stabilized combustion. On the other hand, some experiments did not exhibit this stabilized combustion behavior. In experiments that resulted in two-phase oxygen flow with a large void ratio, such as slug flow, to the fuel, flame-spreading combustion was observed. However, all the experiments that supplied liquid phase or low void ratio oxygen flow achieved a stabilized combustion, and flame-spreading combustion did not occur, even if the oxidizer port velocity was relatively low.

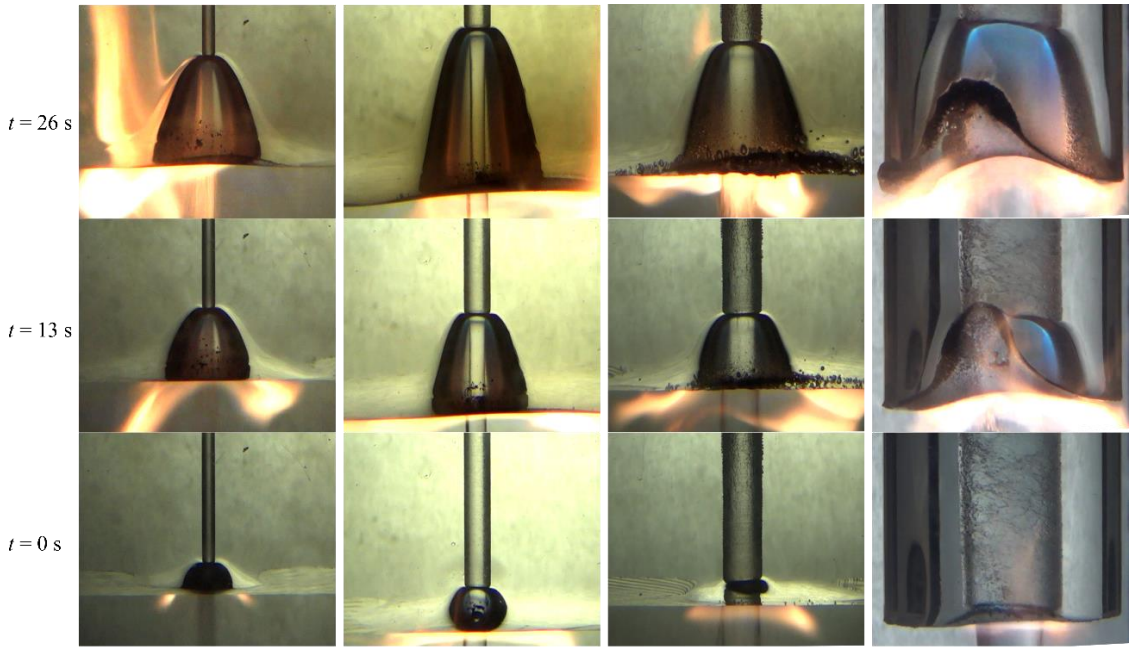

Fig.3.1 Pictures of the combustion state with liquid oxygen and PMMA fuel.

3.2. Extinction and Abnormal Regression

Not only stabilized and flame-spreading combustion, but also extinction and abnormal regression occurred in some experiments. Figure 3.2 shows the experimental conditions of port diameter and oxidizer port velocity when extinction and abnormal regression were observed, and the standard bell-shape regression in stabilized combustion occurred under atmospheric pressure. The bell-shape regression corresponds to the normal regression in the figure.

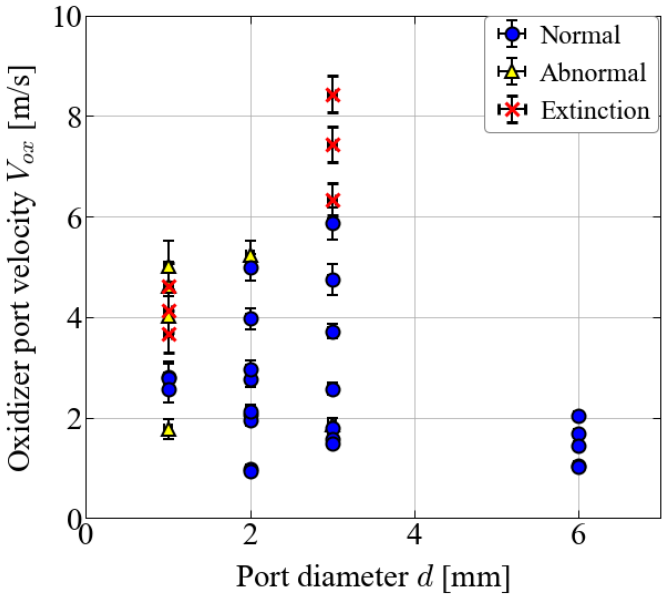

Fig.3.2 Experimental conditions when extinction and abnormal regression occurred under atmospheric pressure.

This figure shows that extinction and abnormal regression occurred with a small port diameter and high oxidizer port velocity. Figures 3.3 and 3.4 are the picture of which extinction occurred. Figure 3.3 shows the combustion state before flame extinction occurred, and Fig. 3.4 is the picture of the fuel end surface after firing.

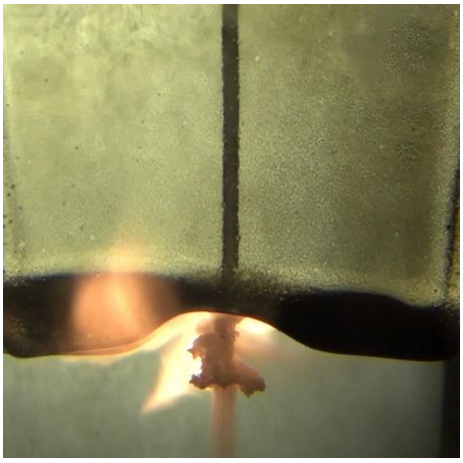

Fig.3.3 Picture of unstable combustion before extinction occurred.

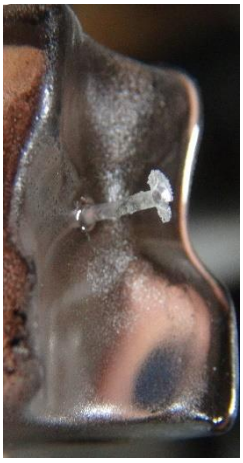

Fig.3.4 Fuel end surface when extinction occurred.

These figures show that a skinny tube-shaped unburned fuel section protruding from the port exit during, and remaining after firing. Figure 3.3 also suggests that liquid oxygen flowed through the skinny tube during firing. Before extinction, the diffusion flame was sustained around the port exit for a while after ignition did not make the fuel duct regress like a bell-shape as seen in the normal regression. Instead, the entire fuel end surface regressed uniformly, scorched by unstable diffusion flame. Before extinction, the axial fuel regression rate was almost zero, even though the normal regression rate in stabilized combustion was relatively slow. In a previous study, Murakami investigated the blow-off of stabilized combustion with gaseous oxygen, revealing that the high-speed oxygen gas flowing over the leading edge of the diffusion flame caused blow-off [34]. On the other hand, the extinction observed in these experiments occurred even if the diffusion flame attached to the fuel port exit, which was different from the blow-off phenomenon with gaseous oxygen. Yokoi, who investigated stabilized combustion sustained in a narrow single port fuel, reported that when port diameter was below 0.2 mm and the ambient pressure was atmospheric, quenching occurred due to cold-wall effect [35]. Accordingly, the extinction in this liquid oxygen research seems to be due to the lack of decomposed fuel chemical species.

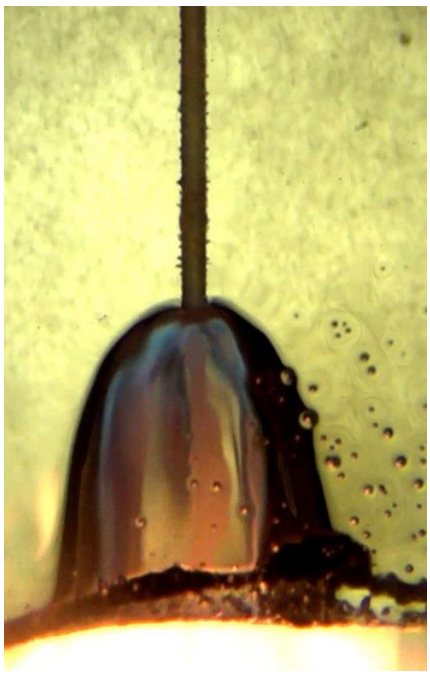

Fig.3.5 Picture of abnormal regression.

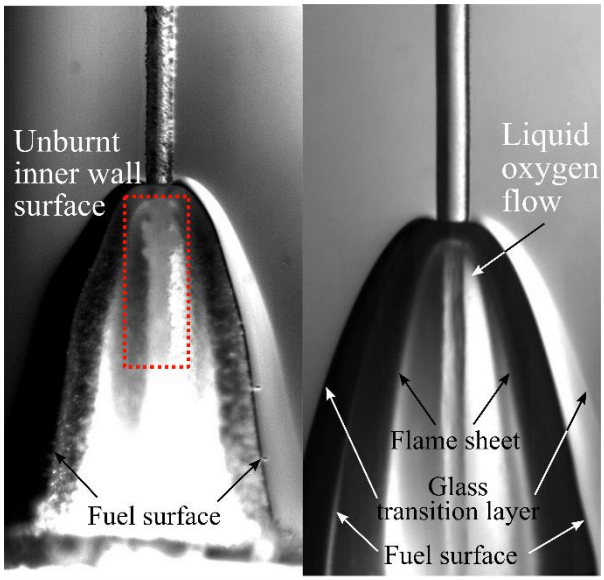

(a) Abnormal regression
d =1.0 mm
V_{ox} =5.0 m/s

(b) Normal regression
d =1.0 mm
V_{ox} =2.8 m/s

Fig.3.6 Comparison of enlarged view between abnormal regression and normal regression captured by high speed camera.

Figure 3.5 shows abnormal regression during firing, and Fig. 3.6 compares the enlarged view between abnormal regression and normal regression captured by a high-speed camera. The axial fuel regression rate in abnormal regression was higher than in extinction but smaller than in normal regression, and the fuel duct regressed in a similar bell-shape in the normal regression. However, the regression shape was not axisymmetric as in normal regression, but rather was distorted. The diffusion flame was sometimes unstable, and sometimes stable when the same skinny tube structure was observed at the tip of every fuel duct as, shown inside the red rectangle of Fig. 3.6 (a). The skinny tube did not appeared in normal regression cases, for example in Fig. 3.6 (b), meaning that the skinny tube is a structure unique to extinction and abnormal regression. It seems that the fuel duct's inner surface could not reach the decomposition temperature and burn due to strong cooling by liquid oxygen. Since liquid oxygen flows through the remained skinny tube, the tube protected liquid oxygen from diffusion flame and vaporization, and oxygen comes from the tube's crack or exit downstream to the flame. Because the flame moves far away from the oxygen exit as the fuel burns in the axial direction, extinction due to insufficient oxygen supply eventually occur. On the contrary, in normal regression, it seems that the tube did not remain or was torn off by liquid oxygen flow because the thickness was smaller than the case when extinction occurred.

3.3. Temperature Distribution around the Tip of Enlarged Fuel Duct

The cooling by liquid oxygen affects axial fuel regression rate in normal combustion as well; i.e., not only in cases of extinction and abnormal regression. Figures 3.7 and 3.8 are the enlarged view of the tip of a fuel duct in stabilized combustion with gaseous oxygen and liquid oxygen, respectively. Figure 3.8 shows the boundary between the black and white sides along the regression surface. This boundary is the glass transition layer of fuel where the reflective index discontinuously changes due to the large variation in density near the glass transition temperature. Therefore, the boundary line corresponds to a kind of isothermal line. It is possible to estimate the temperature distribution inside a fuel by this line. The enlarged duct image of the liquid oxygen case in Fig. 3.8 shows that the curved isothermal line extends along the regressed surface and has a peak located just outer of the unburned port surface. This peak suggests that the most advanced heat penetration position is not on the port wall surface but in the region slightly outside the wall surface in the radial direction.

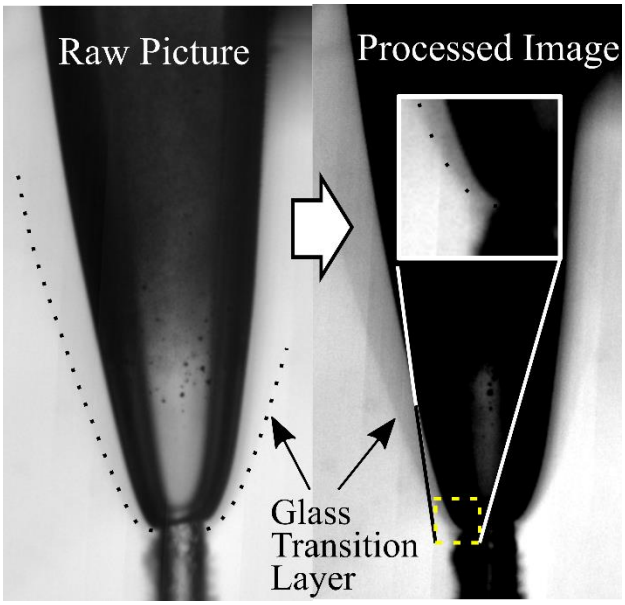

Fig.3.7 Picture around the tip of an enlarged duct supplying gaseous oxygen.

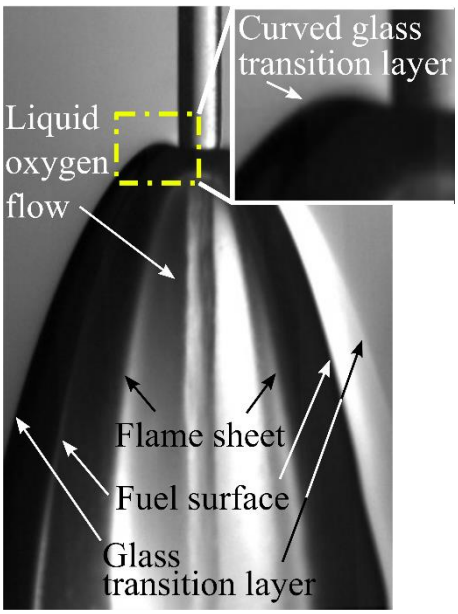

Fig.3.8 Picture around tip of an enlarged duct supplying liquid oxygen shows the temperature distribution in a fuel.

On the other hand, because the isothermal line with gaseous oxygen does not have a peak, the most advanced heat penetration is on the inner port wall surface, as shown in Fig. 3.7. A previous study investigated the temperature distribution inside a fuel bed with air as an oxidizer using holographic interferometry [36]. Though the research supplied air, not gaseous oxygen, the results showed that the

most heated part is the port wall surface, where the diffusion flame heats. However, in the liquid oxygen case, it seems that the diffusion flame cannot directly heat the port wall surface, but only thermal conduction through solid fuel can heat the wall surface. Based on this presumption, it is inferred that a diffusion flame cannot enter into a fuel duct where a liquid phase oxidizer flows; i.e., backfiring shall not occur in AIEB hybrid rockets with liquid oxygen.

CHAPTER 4.

AXIAL FUEL REGRESSION RATE

Axial fuel regression rate is the most critical characteristic for AIEB hybrid rockets because the regression rate determines the fuel grain dimensions required to achieve a specific thrust level. Hashimoto's previous research revealed that the axial fuel regression rate depends on oxidizer port velocity and proportionally increases with increasing chamber pressure, but is independent of port diameter [8]. In this research, the author includes several experiments varying these three parameters individually to investigate each effect on the regression rate. Also, an empirical formula that calculates the regression rate depending on these three parameters is constructed based on the experimental results, and used to study the feasibility of liquid oxygen supplied AIEB hybrid rockets.

4.1. Port diameter and oxidizer port velocity dependences

Dozens of experiments were performed under atmospheric pressure to suppress the chamber pressure fluctuation. These experiments varied oxidizer port velocity from 1.0 to 6.0 m/s for each port diameter to investigate the port diameter and oxidizer port velocity dependences of axial fuel regression rate. Figure 4.1 shows the relation obtained from firing tests between the regression rate, port diameter, and oxidizer port velocity. The figure does not show the experiment results when the liquid oxygen supply became a two-phase flow, and extinction and/or abnormal regression occurred, because it was difficult to measure the regression rate in those cases. In other words, the figure only shows the results of “normal regression” cases. The results show that the regression rate under atmospheric pressure is around 0.2 to 0.5 mm/s; decreasing with increasing oxidizer port velocity and decreasing port diameter. As reported in Hashimoto and Okuda's previous studies [8,16], the results revealed that the regression rate with liquid oxygen has the same trend concerning the oxidizer port velocity dependence, as gaseous oxygen and nitrous oxide cases. However, the results show a port diameter dependence, which did not appear in previous researches with gaseous oxidizers. Accordingly, the port diameter dependence is unique to the regression with liquid oxygen.

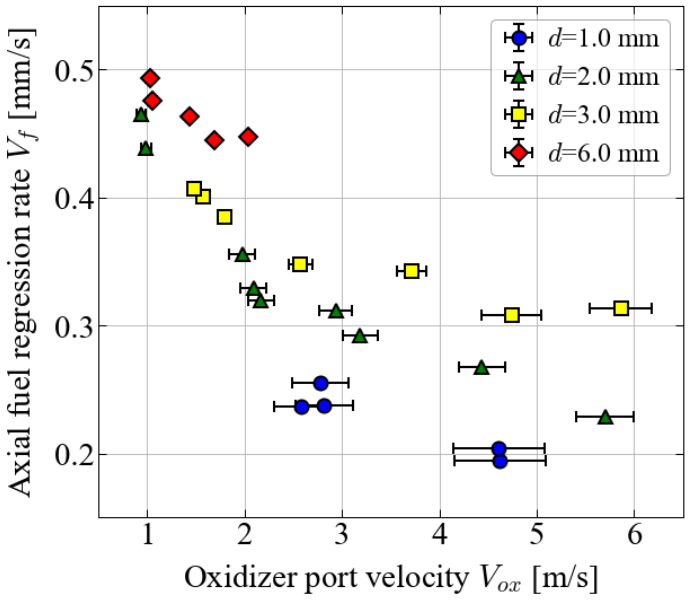

Fig.4.1 Experimental results under atmospheric condition show a dependency of oxidizer port velocity and port diameter on axial fuel regression rate.

4.2. Chamber pressure dependence

The author conducted dozen of the experiments inside a combustion chamber, adjusting the ambient pressure (with Nitrogen) to investigate the chamber pressure dependence of axial fuel regression rate. Oxidizer port velocity was adjusted to around 3.0 m/s in all experiments to reduce the oxidizer port velocity dependence on the regression rate, however the velocity deviated from 3.0 m/s in some experiments due to chamber pressure fluctuations. Even if it was small, chamber pressure fluctuation changed the oxidizer mass flow rate due according to the governing equation of incompressible fluid flow in a pipe/tube. To investigate whether chamber pressure affects the port diameter dependence, the author employed fuels having two different diameters of 1.0 and 2.0 mm. Figure 4.2 (a) and (b) show the relation obtained from experiments between the regression rate and chamber pressure when port diameter was 1.0 or 2.0 mm, respectively. These results revealed that the regression rate increased almost proportionally with increasing chamber pressure, regardless of port diameter. Both determination coefficients calculated by linear regression analysis exceed 0.97. Although the oxidizer port velocity deviated from 3.0 m/s within the range of values: 1.9 to 6.1 m/s, the oxidizer port velocity fluctuation did not affect the regression rate significantly.

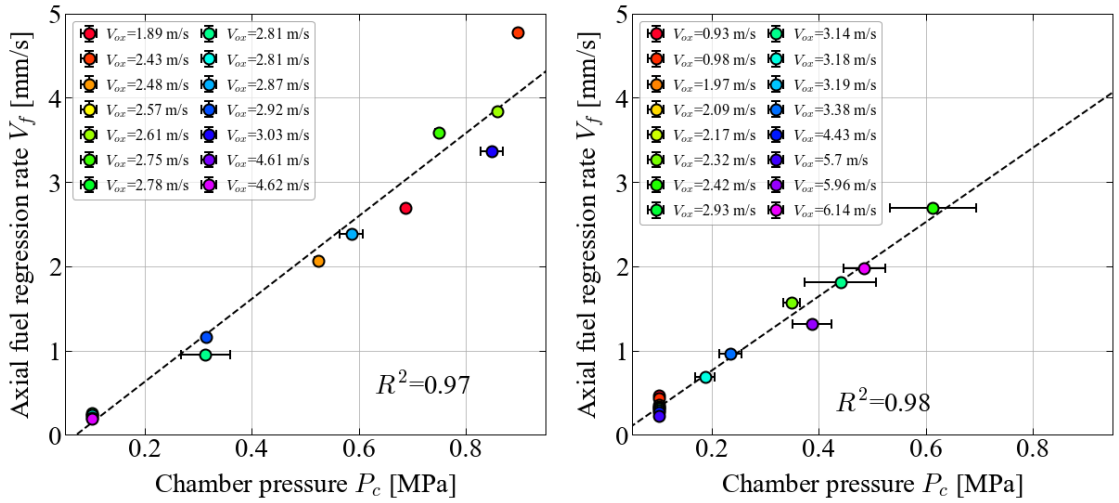

(a) d=1.0 mm (b) d=2.0 mm

Fig.4.2 Experimental results operated in a pressure vessel showed that axial fuel regression rate proportionally increased with increasing ambient pressure.

The results indicate that the oxidizer port velocity dependence is insignificantly small compared to the chamber pressure dependence. Figure 4.3 shows the two results using different port diameters in one graph, using the different makers to identify the port diameter variation.

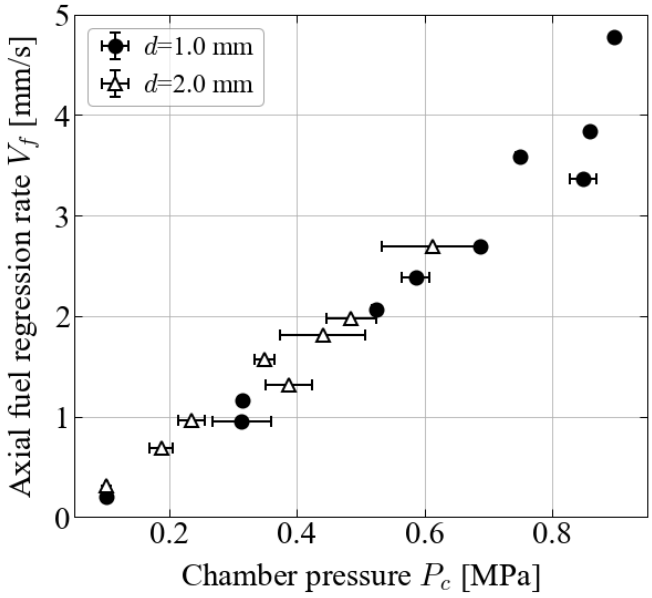

Fig.4.3 Port diameter dependence of axial fuel regression rate is negligibly small compared to the pressure dependence.

The figure shows that the port diameter dependence can be regarded as negligibly small compared to the chamber pressure or oxidizer port velocity dependences because the difference is comparable with the measurement error. Moreover, the figure reveals that chamber pressure did not affect port diameter dependence in the range of 0.1 to 0.6 MPa. The previous section's results support the above discussion because the regression rate variation with varying oxidizer port velocity was less than 0.2 mm/s under atmospheric pressure. Though the range of oxidizer port velocity is not the same, the regression rate with liquid oxygen is 80% in magnitude that with gaseous oxygen [8], and equal in magnitude that of gaseous nitrous oxide [16]. Therefore, these experimental results suggest that liquid oxygen-supplied AIEB hybrid rockets are capable of producing the requisite thrust level of thrust to be used as Earth launch vehicles. For instance, the cylindrical multi-port fuel having 1 mm ports whose diameter is 0.5 m theoretically can produce around 30 kN thrust under 5 MPa of chamber pressure, assuming the rocket motor works at the highest characteristic exhaust velocity conditions. In that case, the axial fuel regression rate reaches approximately 22 mm/s, and the throat diameter should be around 72 mm to achieve that high chamber pressure.

4.3. Constructing an Empirical Formula of Axial Fuel Regression Rate

4.3.1. Empirical Formula

Utilizing the experimental results, which revealed each dependence, the author constructed an empirical formula predicting axial fuel regression rate, V_f, as a function of port diameter, d, oxidizer port velocity, V_{ox}, and chamber pressure, P_c. The formulation used the same function as Eq. 1.1 to estimate the regression rate with gaseous oxygen. Since the regression rate with liquid oxygen has a port diameter dependence, the constructed empirical formula has to treat C_1 and C_2 as experimental coefficients depending on the port diameter. To make the linearization in regression analysis simple, the author assumed that C_1 and C_2 are power functions of port diameter, and constructed the empirical formula as the followings;

$$V_f = \left(\frac{C_1(d)}{V_{ox}} + C_2(d)\right) {P_c}^n \quad (4.1)$$

$$C_1(d) = C_{11} d^{m_1} + C_{12} \quad (4.2)$$

$$C_2(d) = C_{21} d^{m_2} + C_{22} \quad (4.3)$$

where n is a pressure exponent, m_1 and m_2 are port diameter exponents, C_{11} and C_{12} are

empirical constants to give C_1, and C_{21} and C_{22} are the empirical constants to give C_2. Performing non-linear regression analysis gives these seven empirical values from experimental results. The units of the independent variables in the formula are as follows: port diameter, d, is [mm]; oxidizer port velocity, V_{ox}, is [m/s]; chamber pressure, P_c is [MPa]; and axial fuel regression rate, V_f, is [mm/s]. Because, as referred to in Sec. 4.2, the oxidizer port velocity and port diameter dependences are much smaller than the chamber pressure dependence, a slight pressure fluctuation will affect the correlation of empirical constants, except for the pressure exponent. For this reason, the regression analysis to identify the empirical constants consists of two steps; one is for the identification of the pressure exponent, and the other is for the other empirical constants. Iterative calculations are necessary to simultaneously identify all empirical constants with achieving consistency. Step1 solves for the empirical constants other than the pressure exponent using only the experimental results conducted under atmospheric pressure to eliminate pressure measurement error and fluctuation. Then, Step2 solves for the pressure exponent using the other empirical constants identified in Step1. The analysis iteratively conducted these two regression calculations until each constant error converging to a range less than 10^{-5}%. Table 4.1 shows the resulting empirical constants and their standard error. The following sections discuss the accuracy of the constructed empirical formula compared with experimental results.

Table 4.1 Empirical constants.

Empirical constant	Value	Standard error
C_{11}	-1.486	0.027
C_{12}	6.722	0.030
m_1	0.6858	0.0070
C_{21}	4.652	0.987
C_{22}	-2.057	1.025
m_2	0.4008	0.0600
n	1.279	0.032

4.3.2. Empirical constants related to oxidizer port velocity and port diameter

The regression analysis in Step1, which used the experimental results under atmospheric pressure, used a pressure error of 1 kPa as the difference of ground-level atmospheric pressure at each test. To validate the formulation of C_1, C_2, and derive empirical constants except for pressure exponent, the

author compared C_1 and C_2 given by Eq. 4.2 and 4.3 using with those obtained from experiments in each port diameter case. C_1 and C_2 were obtained for each port diameter from experiments conducted under atmospheric pressure at different oxidizer port velocities, in which the calculation utilized linear regression analysis using Eq. 4.2 and 4.3 as a regression line. Table 4.2 shows the experimental coefficient, C_1, C_2, and their standard error. Figure 4.4 compares the experimental coefficients obtained for each port diameter shown as circular plots, and overall trend of Eq. 4.2 and 4.3 using the empirical constants shown as lines.

Table 4.2 Experimental coefficient: C_1 and C_2.

Port diameter	Experimental coefficient		Standard error	
d [mm]	C_1	C_2	σ_{C_1}	σ_{C_2}
1.0	5.23	2.61	1.28	0.41
2.0	4.33	4.04	0.33	0.19
3.0	3.56	5.21	0.29	0.13
6.0	1.64	7.47	0.35	0.26

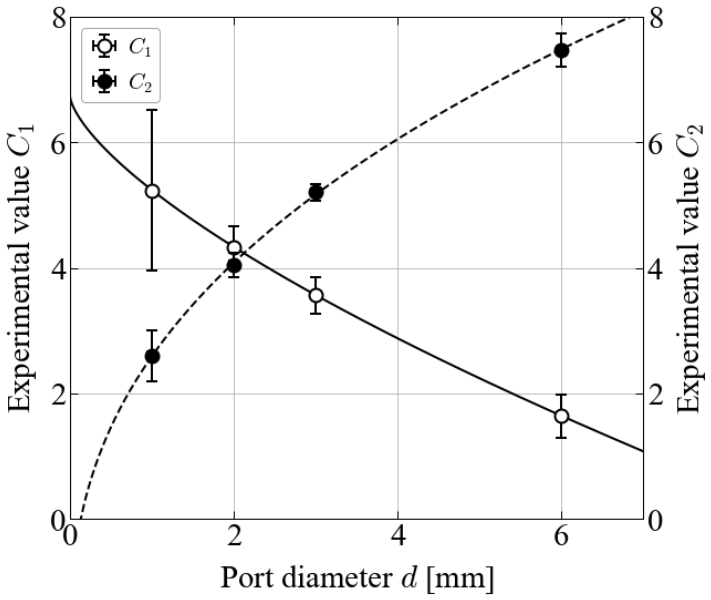

Fig.4.4 Comparison of C_1 and C_2 calculated from the empirical formula for each port diameter.

The figure shows that the experimental coefficient, C_1 and C_2, calculated from the empirical formulas coincide with those obtained from the experimental results for each port diameter. Besides,

the comparison also shows that the coefficient of determination exceeds 0.99. Therefore, it can be said that the assumption that the coefficient, C_1 and C_2, are power functions of port diameter is reasonable. Figure 4.5 shows the comparison between the axial fuel regression rate obtained from experimental results and calculated from the empirical formula, Eq. 4.1 using identified empirical constants.

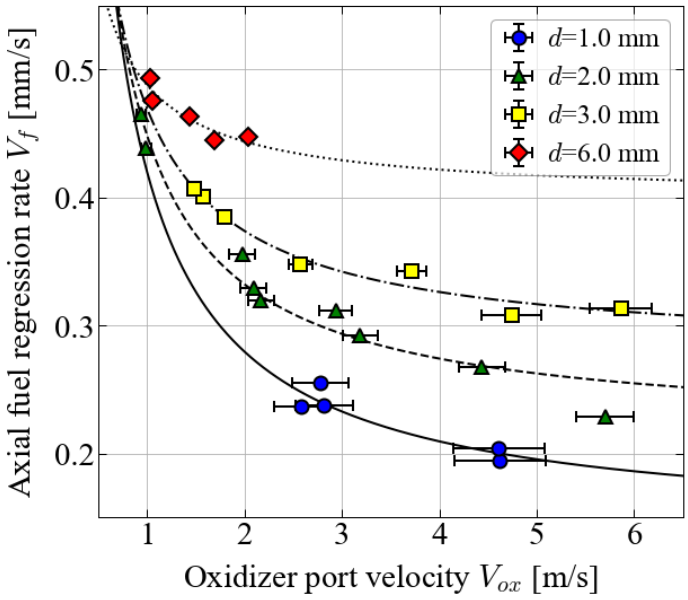

Fig.4.5 Comparison of axial fuel regression rate between calculations using the empirical formula and experimental results.

The calculated regression rate, as shown in the lines, agrees well with the experimental results. Even though the number of the experiments being the port diameter of 1.0 and 6.0 mm is few, the coefficients of determination for port diameter are around 0.84 to 0.97. The comparison shows that the identified constants and constructed formulae have sufficient accuracy in estimating the regression rate under atmospheric pressure. The calculation results also revealed the characteristic of port diameter dependence: the magnitude of port dependence becomes large with decreasing port diameter. However, note that the constructed formulae are inadequate when the oxidizer port velocity is lower than 1.0 m/s, because it gives an incredibly high regression rate as the oxidizer port velocity approaches zero. Also, note that although the calculated regression rate approaches to C_2 with increasing the oxidizer port velocity, extinction eventually occur in reality.

4.3.3. Pressure exponent, n

The regression analysis in Step2 identifies the pressure exponent, n, using the other empirical constants derived in the Step1 analysis. For removing the effect of port diameter and oxidizer port velocity, the regression analysis used the following value derived from Eq. 4.1 as a simple power function of chamber pressure; $V_f(C_1/V_{ox} + C_2)^{-1}$. Figure 4.6 shows the result of regression analysis for pressure exponent. Since the fitted curve given by the calculation using empirical constants agrees well with the experiment results and the coefficient of determination is 0.97, it seems reasonable to conclude that the constructed formulae and empirical constants have sufficient accuracy in estimating the regression rate under pressurized conditions. The resulting pressure exponent is $n \approx 1.26$, which is relatively close to unity, however, larger than the values of n=0.951 and 0.996 reported in previous studies with gaseous oxygen [8,11]. The reason why the exponent exceeds unity is that the regression rate calculated from the empirical formula becomes zero only when chamber pressure is zero. Okuda et al. and Fukada reported the same problem in constructing the empirical formula with gaseous nitrous oxide. They suggested that the pressure exponent becomes close to unity by adding the term of blow-off limit to the empirical formula [16,37]. Similarly, because extinction also occurs in stabilized combustion with liquid oxygen, as referred to in Sec. 3.2, adding the term of extinction to the empirical formula with liquid oxygen might make the pressure exponent close to unity.

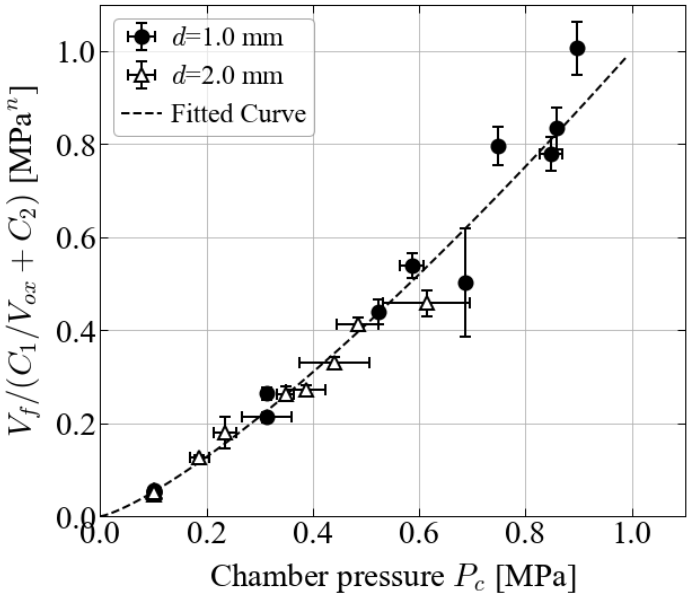

Fig.4.6 Comparison concerning ambient pressure between the results calculated from the empirical formula and the experimental results.

CHAPTER 5.

AXIAL FUEL REGRESSION MODEL

It is necessary to reveal the physical mechanisms of fuel regression to understand the axial fuel regression characteristics in stabilized combustion with liquid oxygen. This chapter introduces a model of axial fuel regression considering the heat energy conservation at the tip of the enlarged fuel duct. The end of this chapter reveals the mechanisms of each dependence on the axial fuel regression rate observed in the experiment using the model. Thanks to the physical model construction, it becomes possible to estimate the regression rate under various conditions in the case not only of the PMMA and liquid oxygen propellant combination, but for combinations as well.

5.1. Model Construction

The axial fuel regression model is constructed by taking the cooling effect of liquid oxygen into account. A portion of the heat supplied from the diffusion flame through gaseous heat conduction transfers to the liquid oxygen flow, while the remaining heat decomposes the fuel. The difference between the amount of heat input and heat loss from the duct tip can be used to calculate the axial fuel regression rate, since axial fuel regression rate is equivalent to the decomposition rate of the fuel duct's tip in the axial direction. For the sake of simplicity, assuming an ideal situation where liquid oxygen flows between parallel fuel plates and stabilized combustion is sustained at the exit, the model considers the balance of heat that comes in and out of the control volume, which moves together with the regressing fuel surface of enlarged duct tip. The control volume is a cube shown as a red square in Fig. 5.1. The cubic control volume size is large enough to neglect the solid heat conduction from the control volume. Specifically, the axial length is long enough, and the radial length is short enough to make the temperature gradient negligibly small at the control volume boundaries. The heat balance equation is the following;

$$\dot{q}_{net} = \dot{q}_{in} - \dot{q}_{cool} \qquad (5.1)$$

Where, $\dot{q}_{cool}$ is the heat flux to liquid oxygen, $\dot{q}_{in}$ is the heat flux from the diffusion flame, and $\dot{q}_{net}$ is the net heat consumption for heating and decomposing solid fuel in unit time. The following sections construct each heat flux model and finally derive the axial fuel regression rate using Eq. 5.1.

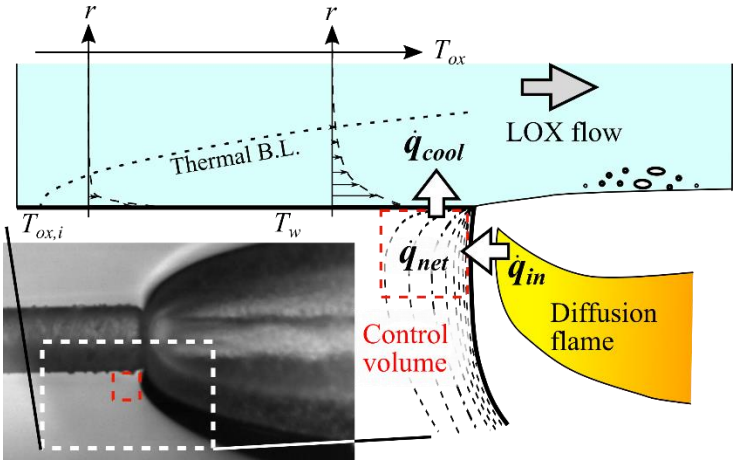

Fig.5.1 Energy conservation in control volume at the tip of the enlarged fuel duct.

5.1.1. Model of Net Heat Consumption, $\dot{q}_{net}$

Net heat consumption, $\dot{q}_{net}$, is the amount of heat expended on raising the temperature of, and decomposing, the fuel coming into the control volume with the inlet velocity of axial fuel regression rate, V_f. Therefore, the following equation gives $\dot{q}_{net}$;

$$\dot{q}_{net} = V_f \left(\int_{T_i}^{T_{dec}} \rho_f c_{p,f} dT + H_{dec} \rho_f |_{T=T_{dec}} \right) \quad (5.2)$$

where, T_i is initial fuel temperature, T_{dec} is fuel decomposition temperature, ρ_f is fuel density, $c_{p,f}$ is fuel specific heat capacity, and H_{dec} is decomposition energy. Stoliarov et al. pointed out that PMMA does not clearly change to the liquid phase until decomposition, and its melting heat is negligibly small [38]. In this study using PMMA as a fuel, the model of $\dot{q}_{net}$ does not consider the melting heat but considers only decomposition heat. Since the fuel density and specific heat capacity change depending on temperature, these two values are functions of temperature, which are given by interpolating the experimental results from Ref. [39,40], as Figs 5.2 and 5.3 show. The fuel decomposition temperature uses T_{dec}= 639.15 K, and the decomposition energy H_{dec} is 870 kJ/kg, reported by Stanislav et al. [38]. Assuming a fuel has been precooled, the initial fuel temperature, T_{in},

is the same as the supplied liquid oxygen temperature.

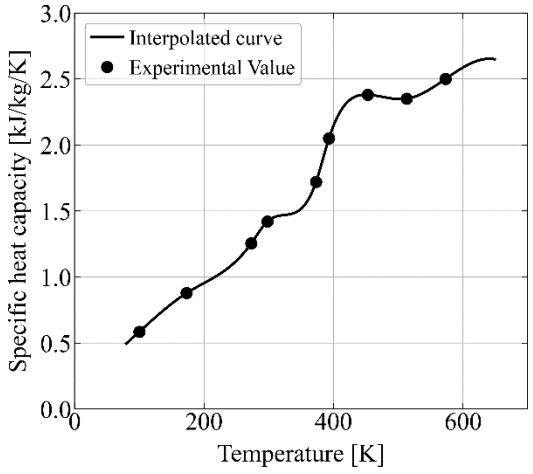

Fig.5.2 Specific heat of PMMA is a function of temperature.

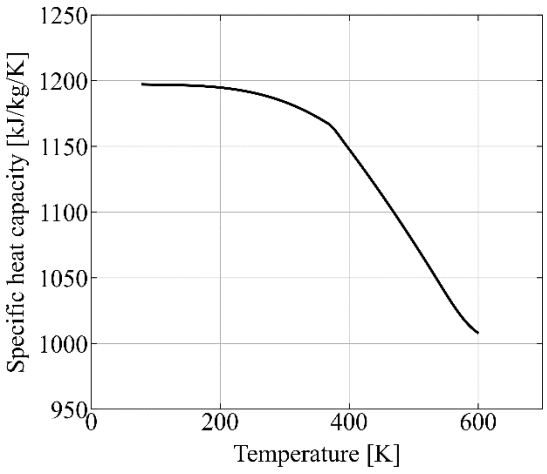

Fig.5.3 Density of PMMA is a function of temperature.

5.1.2. Model of Heat Loss, $\dot{q}_{cool}$

Assuming turbulent heat transfer, heat loss from the control volume to liquid oxygen, $\dot{q}_{cool}$, is calculated from Eq. 5.3, using average Nusselt number, Nu_m;

$$\dot{q}_{cool} = \frac{Nu_m \lambda_{ox}}{d}(\bar{T}_w - T_{ox}) \quad (5.3)$$

where, λ_{ox} is oxidizer thermal conductivity, $\overline{T_w}$ is wall temperature on the control volume, d is port diameter, and T_{ox} is oxidizer temperature. This study assumes $\overline{T_w}$=180 K, because the port wall temperature was not measured in the experiments. Assuming liquid nitrogen precooled the oxidizer through the feed line, the oxidizer temperature uses 80 K, the boiling temperature of liquid nitrogen under atmospheric pressure. The averaged Nusselt number, Nu_m, was calculated from Dittus-Boelter's equation shown as Eq.5.46.3, which assumes a fully developed temperature and velocity boundary layer [41].

$$Nu_m = 0.023Re^{0.8}Pr^{0.4} = 0.023(\rho_{ox}V_{ox}d/\mu_{ox})^{0.8}Pr^{0.4} \quad (5.4)$$

The thermal conductivity and Prandtl number used λ_{ox}=166×10^{-3} W/m·K and Pr=2.42, respectively,

from Ref. [42] as the value of liquid oxygen at 80 K. The calculation of Reynolds number also used the following values listed in Ref.[42]: the density is ρ_{ox}=1190 kg/m3; and the viscosity is μ_{ox}=253.6×10^{-6}.

5.1.3. Model of Heat Input, $\dot{q}_{in}$

Figure 5.5 schematically presents the vicinity around the diffusion-flame tip of stabilized combustion with liquid oxygen.

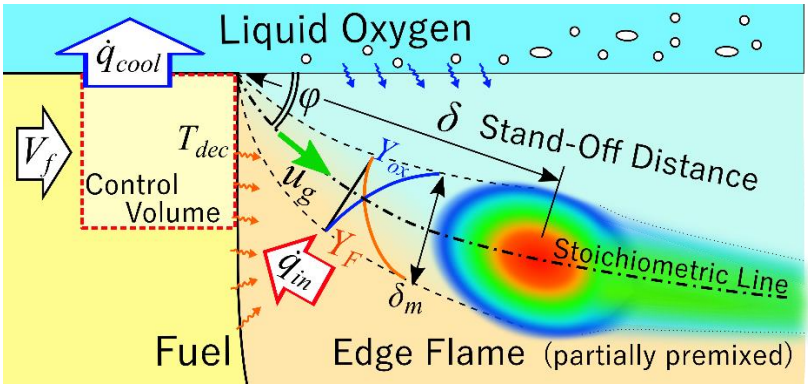

Fig.5.4 Schematic presents the vicinity around the diffusion-flame tip of stabilized combustion with liquid oxygen.

Assuming the radiative heat transfer is negligibly smaller than the heat conduction, the heat flux from the diffusion flame, $\dot{q}_{in}$, can be calculated from Fourie's law shown in Eq.5.5, as simple gas-phase heat conduction through fuel-oxygen mixture gas;

$$\dot{q}_{in} = \frac{\lambda_{ig}}{\delta}(T_b - T_{dec}) \qquad (5.5)$$

where, λ_{ig} is thermal conductivity of fuel-oxygen mixture gas in flame zone, δ is stand-off distance, T_b is adiabatic flame temperature, and T_{dec} is fuel decomposition temperature. This model does not consider the blowing effect making heat transfer to a fuel surface suppress caused by vaporized fuel gas flow for simplicity. Although both phases of the oxidant and the fuel are different from stabilized combustion, the co-axial diffusion flame burner's flame structure, when the burner rim thickness is negligibly thin, is similar to that of the stabilized combustion with liquid oxygen. The diffusion flame's leading edge has a tri-brachial structure called triple-flame [43,44] because partially premixed gas

flows into the leading edge. The previous studies, such as Refs. [45,46], revealed that the leading edge of the diffusion flame spreading on the solid fuel surface also forms triple-flame. However, several studies [47,48] show that when the concentration gradient is steep, such as in a diffusion burner having a thin rim, both lean and rich premixed wings of the tri-brachial structure disappear, and the propagation velocity approaches the laminar premixed burning velocity. The resulting flame is called a flame-edge or edge-flame [49]. Buckmaster and Takahashi et al. suggested the reason is the thickness of the mixing layer δ_m becomes thinner than the quenching distance [50,51]. The $\dot{q}_{in}$ model in this study neglects the mixing time of assuming the leading edge of the diffusion flame with liquid oxygen is an edge-flame, because it is shorter than the chemical reaction time τ_c. Gaseous oxygen vaporized from liquid oxygen and gaseous fuel from the fuel surface generate a premixed gas in the mixing layer. The premixed gas flows with a velocity u_g and ignites after a certain ignition delay τ_c. Now, defining the distance from the fuel surface to the ignition point as a stand-off distance, δ, the distance can be calculated from Eq. 5.6.

$$\delta = u_g \tau_c \qquad (5.6)$$

Mixture gas velocity, u_g, was calculated from using the gaseous fuel mass flux, $\dot{M}_f$, gaseous oxygen mass flux, $\dot{M}_{ox}$, and mixture gas density, ρ_g. Since the diffusion flame is appears at the stoichiometric mixing layer, the gas flowing into the flame leading edge is a stoichiometric mixture. Therefore, stoichiometric oxidizer to fuel ratio, O/F_{st}, can estimate the mixture gas velocity u_g as Eq. 5.7;

$$u_g = \frac{\dot{M}_f}{\rho_g}\left(1 + \frac{\dot{M}_{ox}}{\dot{M}_f}\right) = \frac{R_g T_g}{P_c}\rho_f V_f (1 + O/F_{st}) \qquad (5.7)$$

where, R_g and T_g are the gas constant and the initial temperature of the mixture, respectively. Since ignition delay is a function of chamber pressure, P_c, and ignition temperature of mixture, T_{ig}, it depends on the following values: lower heating value, h_l; the mole fractions of fuel and oxygen, χ_f, χ_{ox}; activation energy, E_a; universal gas constant, R; and overall reaction order, $i + j$. Note that T_{ig} is the temperature where the boundary between pre-heat and reaction zone. It is reasonable to assume that the hydrocarbon fuel's reaction order is around two, and the mixture temperature is almost independent of pressure, oxidizer port velocity, and port diameter. Replacing all of these values as constant to A', the ignition delay, τ_c, is formulated to be Eq. 5.8 by using a constant, A'. Eq. 5.9 is

the definition of A', and A is a unique value to the combination of fuel and oxidizer.

$$\tau_c \approx \frac{A'}{P_c} \quad (5.8)$$

$$A' = \frac{A}{h_l {\chi_f}^i {\chi_{ox}}^j} {T_{ig}}^{i+j+1} \exp\left(\frac{E_a}{R_u T_{ig}}\right) \quad (5.9)$$

Since the mixture gas temperature increases with proximity to the flame leading edge, the estimation for T_{ig} in the above equations uses the average of adiabatic flame temperature T_b and initial mixture temperature T_g. Initial mixture temperature T_g is calculated from the gas temperature, the specific heat capacities of gaseous oxygen and fuel, and the stoichiometric oxidizer to fuel ratio O/F_{st}. Eventually, the ignition temperature T_{ig} can be calculated from Eq. 5.10. The calculation assumes the oxidizer gas temperature $T_{ox,g}$ as the boiling temperature of liquid oxygen at the chamber pressure.

$$T_{ig} = \frac{T_b + T_g}{2} = \frac{1}{2}\left(T_b + \frac{O/F_{st} c_{p,oxg} T_{ox,g} + c_{p,fg} T_{dec}}{O/F_{st} c_{p,oxg} + c_{p,fg}}\right) \quad (5.10)$$

Similarly, the estimation for thermal conductivity of mixture gas in flame zone λ_{ig} uses the average value of combustion gas λ_b and initial mixture gas λ_g. Initial thermal gas conductivity λ_g is calculated from that of gaseous oxygen and fuel, and the stoichiometric oxidizer to fuel ratio O/F_{st}. Eventually, the thermal conductivity of mixture gas λ_{ig} can be calculated from Eq.5.11.

$$\lambda_{ig} = \frac{\lambda_b + \lambda_g}{2} = \frac{1}{2}\left(\lambda_b + \frac{O/F_{st}\lambda_{g,ox} + \lambda_{g,f}}{1 + O/F_{st}}\right) \quad (5.11)$$

Using the physical properties of fuel and oxygen gas and their mass fractions, the gas constant R_g is calculated from Eq. 5.12.

$$R_g = \upsilon_{ox} R_{ox} + \upsilon_f R_f = \frac{R_u}{1 + O/F_{st}}\left(\frac{O/F_{st}}{M_{ox}} + \frac{1}{M_f}\right) \quad (5.12)$$

where, υ_f and υ_{ox} are the mass fraction of fuel and oxygen, R_u is the universal gas constant, M_{ox} and M_f are the molar mass of fuel and oxygen. For the fuel molar mass, M_f, the molar mass of methyl methacrylate (MMA) was used from the assumption that PMMA decomposes to monomer

methyl methacrylate. These thermophysical properties of fuel and oxygen used the values at its decomposition and boiling temperature, respectively. Substituting Eqs. 5.6, 5.7, and 5.8 into Eq. 5.5 formulates the heat input, $\dot{q}_{in}$, from diffusion flame to fuel duct tip as Eq. 5.13.

$$\dot{q}_{in} = \frac{\lambda_g (T_b - T_{dec}) {P_c}^2}{A' \rho_f (1 + O/F_{st}) R_g T_g V_f} \quad (5.13)$$

Since it is challenging to calculate the constant A' related to ignition delay, the value of A' = 70.0 Pa·s was chosen to correspond with the experimental result roughly.

5.1.4. Analytical Solution of Axial Fuel Regression Rate

The three kinds of heat flux were formulated in the above sections as Eq. 5.2, 5.3, and 5.13. Note that the axial fuel regression rate, V_f, appears in the net heat consumption term, $\dot{q}_{net}$, and also the input term, $\dot{q}_{in}$. Substituting these three heat flux terms into the heat valance equation, Eq. 5.1 and analytically solving the equation derive the axial fuel regression as the following:

$$V_f = \frac{1}{2Q_{net}} \left(\sqrt{\dot{q}_{cool} + 4Q_{net}Q_{in}} - \dot{q}_{cool} \right) \quad (5.14)$$

Eq. 5.14 introduced new quantities, Q_{net} and Q_{in}, to simplify the notation. Q_{net} is the value obtained by dividing $\dot{q}_{net}$ by V_f, which means the volumetric heat consumption, and has a unit of [J/kg]. Q_{in} is $\dot{q}_{in}$ multiplied by V_f. The definition of these two quantities are the following:

$$Q_{in} = \dot{q}_{in} V_f = \frac{\lambda_g (T_b - T_{dec}) {P_c}^2}{A' \rho_f (1 + O/F_{st}) R_g T_g} \quad (5.15)$$

$$Q_{net} = \frac{\dot{q}_{net}}{V_f} = \int_{T_i}^{T_{dec}} \rho_f c_{p,f} dT + H_{dec} \rho_f |_{T=T_{dec}} \quad (5.16)$$

Since the analytical solution of the axial fuel regression rate was derived, the regression rate can be calculated from material properties or experimental conditions. Table 5.1 lists the values used to calculate the axial fuel regression rate with liquid oxygen.

Table 5.1 List of model parameters.

Parameter	Symbol	Value	Unit	Ref.
Oxidizer density	ρ_{ox}	1190	kg/m^3	[42]
Oxidizer viscosity	μ_{ox}	253.6	μPa·s	[42]
Oxidizer Prandtl number	Pr	2.426	–	[42]
Oxidizer thermal conductivity	λ_{ox}	166.1	mW/m·K	[42]
Oxidizer temperature	T_{ox}	80	K	–
Averaged port wall temperature	$\bar{T}_w$	180	K	–
Initial fuel temperature	T_i	80	K	–
Fuel decomposition temperature	T_{dec}	639	K	[38]
Heat of decomposition	H_{dec}	870	kJ/kg	[38]
Empirical constant	A'	70.0	Pa·s	–
Stoichiometric mixture ratio	O/F_{st}	1.92	–	–
Adiabatic flame temperature	T_b	3070	K	[52]
Combustion gas thermal conductivity	λ_b	315	mW/m·K	[52]
Oxidizer molar mass	M_{ox}	32.0	g/mol	–
Fuel gas molar mass	M_f	100.12	g/mol	–
Oxidizer gas thermal conductivity	$\lambda_{ox,g}$	8.87	mW/m·K	[42]
Fuel gas thermal conductivity	$\lambda_{f,g}$	49.9	mW/m·K	[53]
Oxidizer gas specific heat capacity	$c_{p,oxg}$	0.953	kJ/kg·K	[42]
Fuel gas specific heat capacity	$c_{p,fg}$	1.491	kJ/kg·K	[54]
Oxidizer gas temperature	$T_{ox,g}$	90	K	–
Solid fuel density	ρ_f	Fig. 5.3	kg/m^3	[40]
Solid fuel specific heat capacity	$c_{p,f}$	Fig. 5.2	J/kg·K	[40]

Combustion gas thermal conductivity in stoichiometric condition λ_b and adiabatic flame temperature T_b were calculated by NASA chemical equilibrium with applications (NASA-CEA)[52]. The adiabatic flame temperature in regression rate calculations was assumed to be T_b=3070 K, at stoichiometric condition. Figures 5.5 and 5.6 show each relation of adiabatic flame temperature and combustion gas thermal conductivity to mixture ratio when assigned the calculating condition shown in Table 5.2. The equilibrium calculation assumes the fuel is MMA, whose standard enthalpy of formation was calculated utilizing Benson group increment theory [55]. The calculation considers each latent heat of oxidizer and fuel for enthalpy balance consistency, assuming oxygen as a liquid phase

with 90 K heated up from an initial temperature of 80 K and fuel as a gas phase with decomposition temperature 639 K.

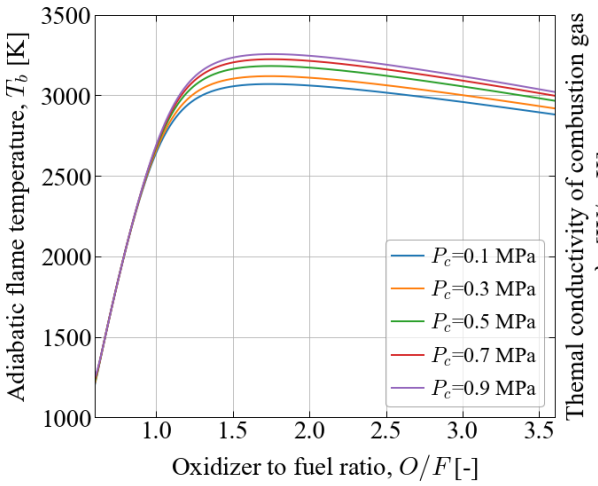

Fig.5.5 The relation between adiabatic flame temperature and mixture ratio.

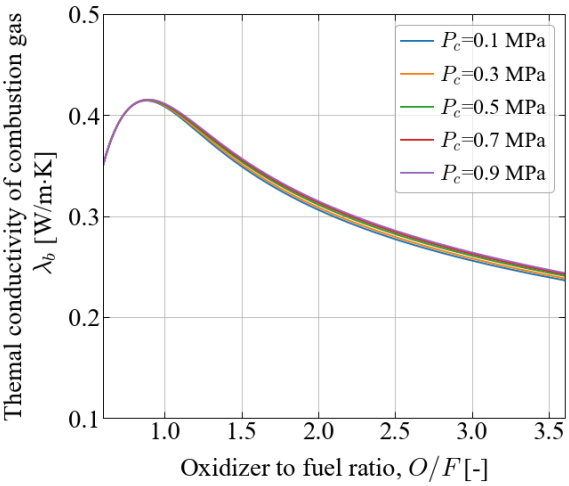

Fig.5.6 The relation between combustion gas thermal conductivity and mixture ratio.

Table 5.2 Calculating condition with PMMA and LOX combination for NASA-CEA.

Parameter	Value	Unit
Oxidizer initial temperature	90	K
Fuel gas initial temperature	639	K
Fuel gas standard enthalpy of formation	-468.3	kJ/mol
The number of carbon atoms in unit fuel molecule.	5.0	mol/mol
The number of hydrogen atoms in a unit fuel molecule	8.0	mol/mol
The number of oxygen atoms in a unit fuel molecule	2.0	mol/mol

5.2. Comparison of the Experiment and Model

This section validates the model through a comparison with experimental results. Firstly, the calculation results compared with the experiment varying chamber pressure conditions are shown below to confirm the model's chamber pressure dependence. Figure 5.7 shows the calculation results as lines when the port diameter is 2.0 mm, and the oxidizer port velocity varied between 1.0, 2.0, and 3.0 m/s. Figure 5.8 shows the results as lines when the oxidizer port velocity is 3.0 m/s, and the port diameter varied between 1.0, 2.0, and 3.0 mm. Both figures show that the calculation results agree well with the experimental data. This good agreement is because the constant A' for ignition delay was selected so as to be consistent with the experiment. As shown in Fig. 5.9, the linear relation between the regression rate and the chamber pressure keeps even if A' is a different value. Only the magnitude of the pressure dependence changes.

Next, the calculation results are compared with the experiment results for varying oxidizer port velocity and under the several port diameter conditions are shown below to confirm the model's dependence of port diameter and oxidizer port velocity. Figure 5.10 shows the calculation results as lines and experimental data under atmospheric pressure as plots when the port diameter varied 1.0, 2.0, 3.0, and 6.0 mm, and the oxidizer port velocity varied from 0.5 to 6.5 m/s. In this figure, the calculation results do not coincide well with the experimental data showing that magnitudes of both the port diameter and oxidizer port velocity dependences are smaller than that of the experiment. However, the calculated curves agree well with the trends in the experimental data. Because of the agreement of the trends that the port diameter dependence increases with decreasing diameter, and the oxidizer port velocity dependence decreases with increasing velocity shows that the modeling of each heat transfer phenomenon is not significantly wrong.

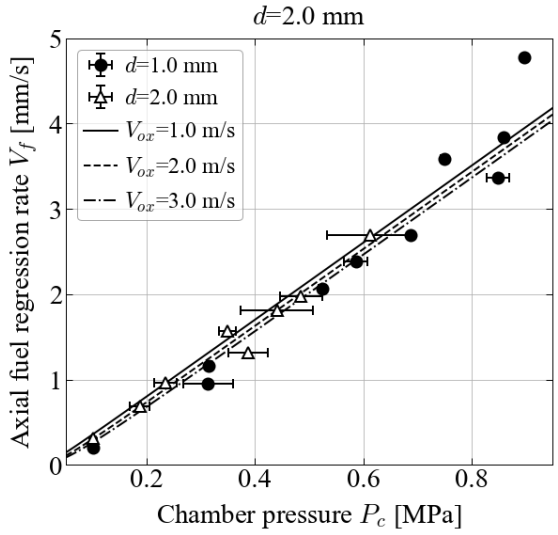

Fig.5.7 Comparing the chamber pressure dependence of axial fuel regression rate between model and experiment, when oxidizer port velocity, V_{ox}, are 1.0, 2.0, and 3.0 m/s.

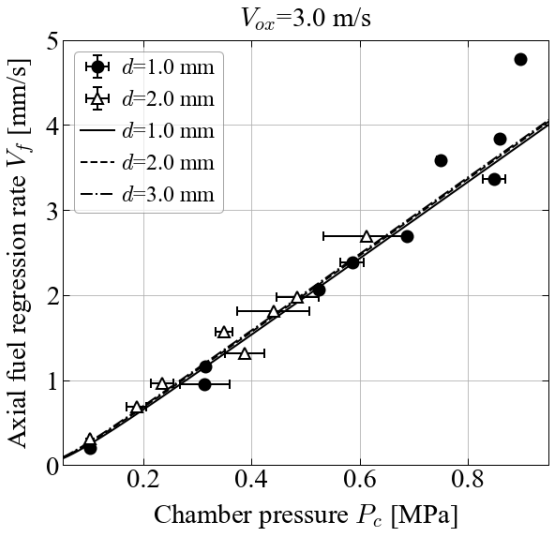

Fig.5.8 Comparing the chamber pressure dependence of axial fuel regression rate between model and experiment, when port diameter, d, are 1.0, 2.0, and 3.0 mm.

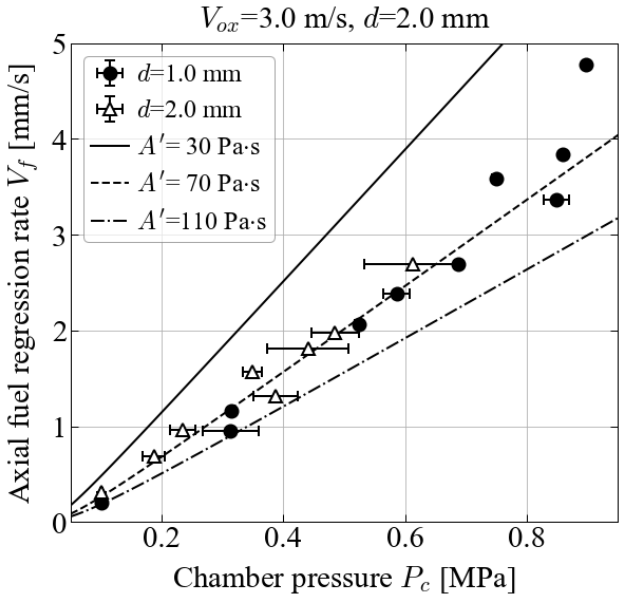

Fig.5.9 Even when changing empirical constant, A', the model maintains the linear correlation between axial fuel regression and chamber pressure.

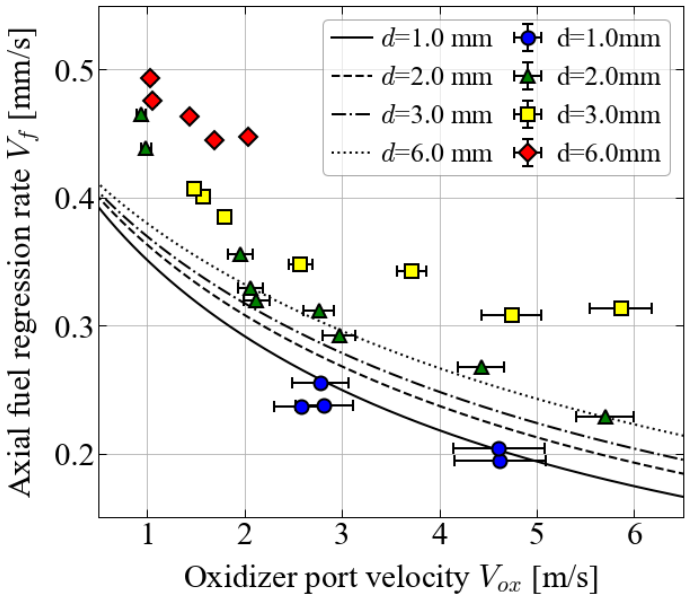

Fig.5.10 Comparing the oxidizer port velocity and port diameter dependences of axial fuel regression rate between model and experiment under atmospheric condition.

5.3. Mechanisms of Each Dependence of Axial Fuel Regression Rate

As the comparison in the previous section shows, the constructed model coincides qualitatively but not quantitatively with experimental data. Because the model agrees well with the trend in the experiment, the model is valuable enough to understand the physical mechanisms causing each dependence. In the following sections, the mechanisms are revealed by using the constructed model.

5.3.1. Chamber Pressure Dependence

This section reveals why the regression rate increases proportionally with increasing chamber pressure, focusing on the relationship between heat input and chamber pressure. Figure 5.11 shows the relationship of heat input, $\dot{q}_{in}$, heat loss, $\dot{q}_{cool}$, and stand-off distance, δ to chamber pressure, P_c, calculated by the model. The calculation condition is that the port diameter is 2.0 mm, and the oxidizer port velocity is 3.0 m/s. As indicated in the figure, heat input proportionally increases with increasing chamber pressure. Based on Eqs. 5.5, 5.6 and 5.8, the reason is that the ignition delay, τ_c, is inversely proportional to chamber pressure, which causes stand-off distance, δ, to decrease, and heat input, $\dot{q}_{in}$, to increase. On the other hand, as indicated in the figure, heat loss does not change with the change in oxidizer port velocity changes. As shown in the heat balance equation: Eq. 5.1, the difference between heat input and heat loss determines the regression rate. Therefore, the heat input increases proportionally to chamber pressure, causing the pressure dependence, and that heat loss does not affect the dependence.

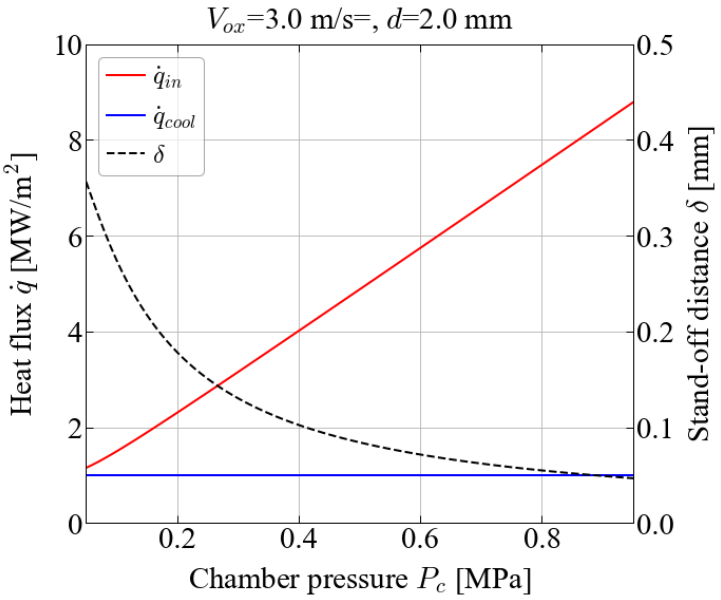

Fig.5.11 Heat input, $\dot{q}_{in}$, proportionally increases with increasing chamber pressure, P_c, because stand-off distance, δ, is inversely proportional to chamber pressure, P_c.

5.3.2. Oxidizer Port Velocity Dependence

This section reveals why the regression rate decrease with increasing oxidizer port velocity by using the same manner in the above section. Figure 5.12 shows the dependences of heat loss, $\dot{q}_{cool}$, and axial fuel regression rate, V_f, to oxidizer port velocity, V_{ox}, from the model when the port diameter is 2.0 mm and the chamber pressure is 0.1 MPa. The figure indicates that both heat input and heat loss increase with increasing oxidizer port velocity, and their difference gradually decreases to a constant value. The increasing rate of heat loss, $\dot{q}_{cool}$, is large for low oxidizer port velocity, and the rate decreases as oxidizer port velocity increases. This is because the averaged Nusselt number, Nu_m, calculated from Dittus-Boelter's equation: Eq. 5.4, depends on oxidizer port velocity V_{ox} of $Nu_m \propto {V_{ox}}^{0.8}$. The heat input, $\dot{q}_{in}$, increases with increasing oxidizer port velocity because the mixture gas velocity u_g decreases with decreasing fuel decomposition rate due to the cooling effect. Figure 5.13 shows the dependence of heat input $\dot{q}_{in}$ stand-off distance δ and mixture gas velocity u_g on oxidizer port velocity V_{ox}. This figure indicates that, with increasing oxidizer port velocity, heat input, $\dot{q}_{in}$, increases and mixture gas velocity u_g and stand-off distance δ decrease. As Eq. 5.7 shows, mixture gas velocity u_g is proportional to the gasified fuel rate, which means mixture gas velocity is proportional to axial fuel regression rate: $u_g \propto V_f$. Considering also the following relations: $\dot{q}_{in} \propto {u_g}^{-1}$ and $V_f \propto {V_{ox}}^{-1}$, the model tells that heat input is proportional to oxidizer port velocity, $\dot{q}_{in} \propto$

V_{ox}. Due to the slight difference in the dependence of oxidizer port velocity on the heat loss and heat input, the regression rate is high for oxidizer port velocity where the difference is large, and the regression rate is low for high oxidizer port velocity as the difference is small.

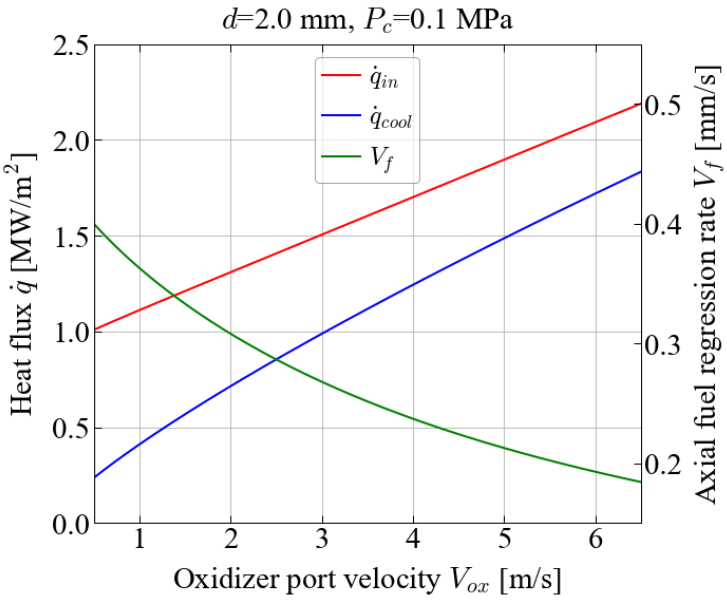

Fig.5.12 Both heat input, $\dot{q}_{in}$, and heat loss, $\dot{q}_{cool}$, increase with increasing oxidizer port velocity, V_{ox}, and the difference gradually becomes smaller.

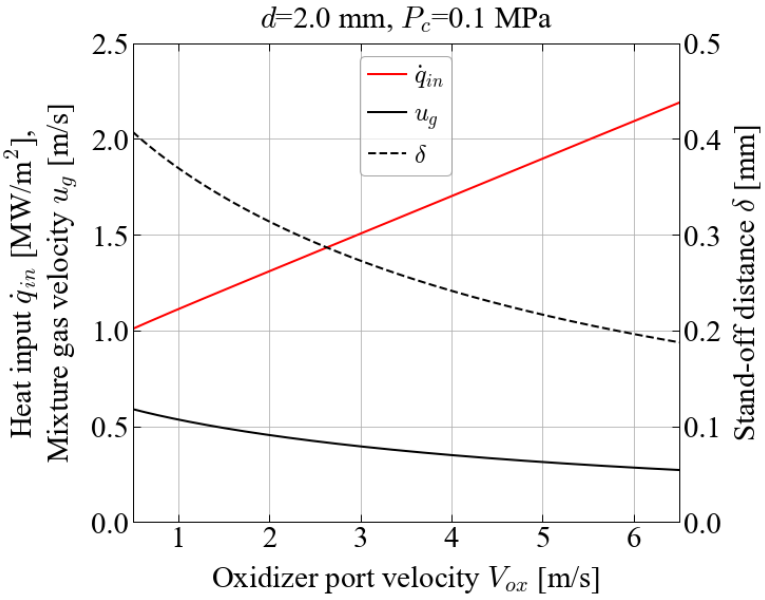

Fig.5.13 Heat input, $\dot{q}_{in}$, increases with increasing oxidizer port velocity because mixture gas velocity decreases with decreasing axial fuel regression rate.

5.3.3. Port Diameter Dependence

This section reveals the causes of port diameter dependence on axial fuel regression rate, and why the regression rate with gaseous oxygen do not exhibit this dependence. Figure 5.14 shows the dependences of heat input $\dot{q}_{in}$, heat loss $\dot{q}_{cool}$, and net heat consumption $\dot{q}_{net}$ on port diameter d when oxidizer port velocity is 1.0 and 6.0 m/s as calculated by the model. The calculation result indicates that both heat input and heat loss increase with decreasing port diameter. Similarly, net heat consumption: namely, the difference between these heat flux, also gradually decreases, and the decreasing rate of net heat consumption increases with decreasing port diameter. Therefore, the magnitude of port diameter dependence becomes large with decreasing port diameter because the increasing rate of heat loss is slightly larger than that of heat input when port diameter decreases. Heat loss increases with decreasing port diameter because a smaller port diameter promotes the heat transfer from fuel to liquid oxygen. From Eqs. 5.3 and 5.4 related to heat loss, the following relations between port diameter and heat loss: $\dot{q}_{cool} \propto d^{-0.2}$, states the mechanism mentioned above. Heat input increases with decreasing port diameter, because, as described in Sec. 5.3.2, suppressed fuel decomposition rate causes decreasing mixture gas velocity due to the increase in heat loss associated with the decreasing port diameter.

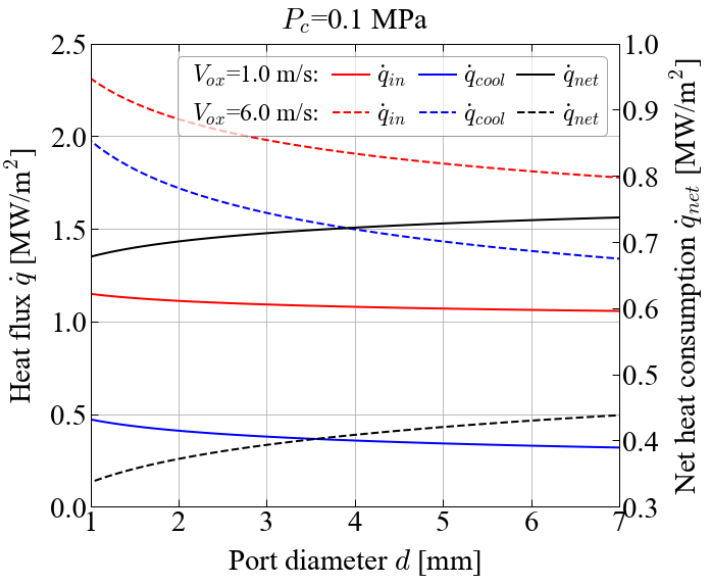

Fig.5.14 The difference between heat input, $\dot{q}_{in}$, and heat loss, $\dot{q}_{cool}$, decreases with decreasing port diameter, d, and the decreasing rate gradually becomes large.

To quantitatively evaluate the magnitude of influence of port diameter on flame spread rate, we introduce a partial derivative of flame spread rate with respect to port diameter, $\partial V_f/\partial d$. When Eq. 5.14 is partially differentiated, the following equation, Eq. 5.17, is derived. Because the order of $\left(\dot{q}_{cool}{}^2 + 4Q_{net}Q_{in}\right)^{-0.5}$ is around 10^{-5}, this term is negligible as $\left(\dot{q}_{cool}{}^2 + 4Q_{net}Q_{in}\right)^{-0.5} \ll 1$. Therefore, the derivative can be calculated from $\dot{q}_{cool}$ and Q_{net}.

$$\frac{\partial V_f}{\partial d} = \left[1 - \left(\dot{q}_{cool}{}^2 + 4Q_{net}Q_{in}\right)^{-0.5}\right]\left(\frac{-1}{2Q_{net}}\frac{\partial \dot{q}_{cool}}{\partial d}\right) \approx \frac{-1}{2Q_{net}}\frac{\partial \dot{q}_{cool}}{\partial d} \qquad (5.17)$$

Then, using Eqs. 5.3, 5.4 and 5.16, the derivative is transformed into the following:

$$\frac{\partial V_f}{\partial d} \approx \frac{0.0023\lambda_{ox}Pr^{0.4}\nu^{-0.8}(\bar{T}_w - T_{ox})V_{ox}{}^{0.8}d^{-1.2}}{\int_{T_i}^{T_{dec}}\rho_f c_{p,f}dT + H_{dec}\rho_f|_{T=T_{dec}}} \qquad (5.18)$$

Figure 5.15 shows the relations of port diameter sensitivity to both port diameter and oxidizer port velocity calculated by Eq. 5.18, assuming atmospheric pressure condition. The figure indicates that the port diameter sensitivity exponentially increases with decreasing port diameter and increases with increasing oxidizer port velocity, as mentioned before in this section. Equation 5.18 also indicates other parameters that affect the port diameter sensitivity, such as an oxidizer thermal conductivity, λ_{ox}. The heat transfer from fuel to oxidizer should occur when gaseous oxygen is supplied, and the heat transfer mode is the same with liquid oxygen; turbulent heat transfer. Therefore, using Eq. 5.18 we can investigate why the port diameter dependence does not appear when gaseous oxygen case is used instead of liquid oxygen case.

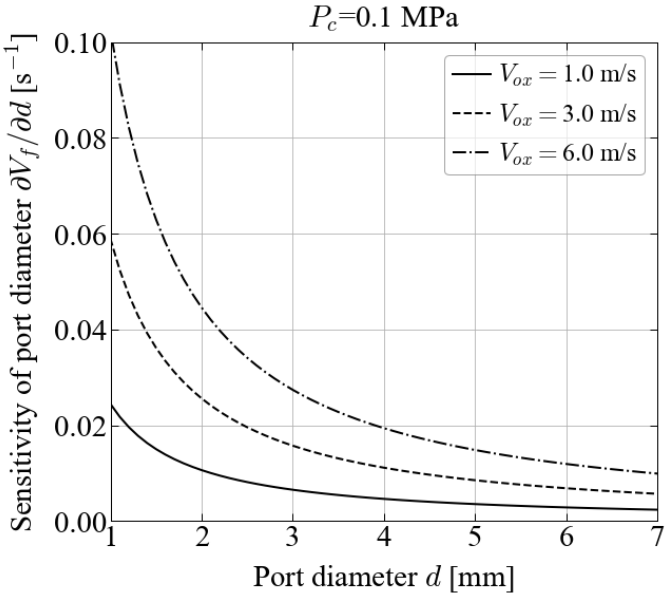

Fig.5.15 Sensitivity of port diameter on axial fuel regression rate exponentially increases with decreasing port diameter, d, and the magnitude becomes large in high oxidizer port velocity, V_{ox}.

Table 5.3 shows other parameters' ratios between gaseous and liquid oxygen, and their exponent values that affect the port diameter sensitivity except for port diameter and oxidizer port velocity. In the table, when gaseous oxygen is supplied, the port wall surface temperature assumes $\bar{T}_{w,GOX}$=580 K, and initial fuel temperature and oxidizer temperature assumes $T_{ox,GOX}$=280 K.

Table 5.3 Parameter ratio of gaseous oxygen to liquid oxygen and exponent values in Eq. 5.18.

Parameter	Symbol	Value of ratio	Exponent of parameter	Value of GOX	Unit
Thermal conductivity	$\lambda_{ox,GOX}/\lambda_{ox,LOX}$	0.15	1	24.77	W/m·K
Prandtl number	Pr_{GOX}/Pr_{LOX}	0.30	0.4	0.7254	–
Kinematic viscosity	ν_{GOX}/ν_{LOX}	66	-0.8	0.142	μm^2/s
Temperature difference between oxidizer and wall	$\dfrac{\bar{T}_{w,GOX}-T_{ox,GOX}}{\bar{T}_{w.LOX}-T_{ox,LOX}}$	3	1	300	K
Volumetric heat consumption	Q_{net}	0.89	1	1719	MJ/m^3

The table shows that the ratio of kinematic viscosity is noticeably larger than the others. Considering the effect of its exponent value also shows that the difference in kinematic viscosity between gaseous

oxygen and liquid oxygen has the greatest impact on port diameter sensitivity difference. Furthermore, the port diameter sensitivity with gaseous oxygen calculated from Eq. 5.18 is around 10^{-2} smaller than that of liquid oxygen even when the oxidizer port velocity is 30 m/s. Therefore, the reason why the port diameter dependence does not appear with gaseous oxygen seems to be mainly due to large kinematic viscosity.

5.3.4. Relation of Heat Loss to Extinction and Abnormal Regression

As described earlier, when extinction and abnormal regression occurred, a skinny tube-shaped portion of unburned fuel formed at the fuel port exit in almost all of the experiments. It seems that the heat loss calculated from the model can estimate the threshold heat flux between extinction and normal regression, since a strong cooling effect by liquid oxygen causes these phenomena. Figure 5.16 shows the heat loss contour map calculated from Eq. 5.13 with the experimental result. According to the figure, the boundary between extinction or abnormal regression and normal regression is close to the contour map. The boundary locates on the heat loss line around 1.4 ~ 1.6 MW/m^2. This result suggests that extinction and abnormal regression would occur when heat loss flux exceeds a specific value. However, when the port diameter is 1.0 mm, the boundary is smaller than the calculated threshold heat loss flux because the model tends to calculate the effect of oxidizer port velocity and port diameter on the regression rate lower than the experiment. If the model can estimate heat loss more precisely, especially the decrease in heat flux for low oxidizer port velocity, the calculated heat loss flux would coincide with the experimentally obtained boundary.

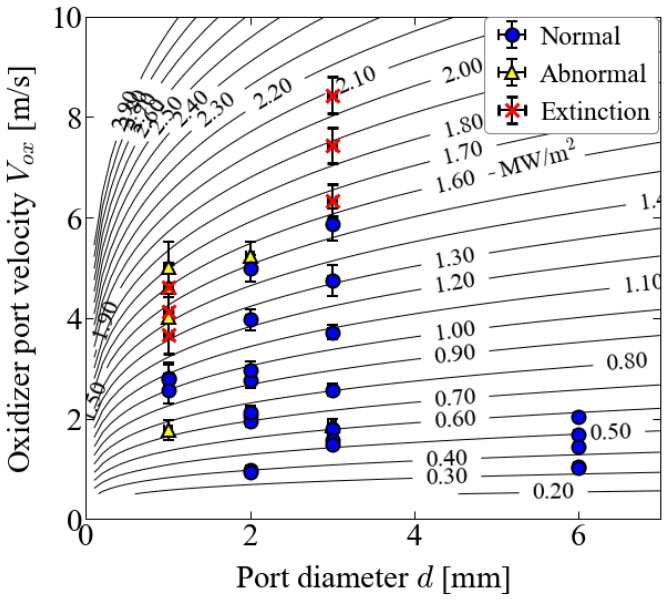

Fig.5.16 Contour map of heat loss, $\dot{q}_{cool}$, shows the boundary between normal stabilized combustion and extinction or abnormal regression.

5.4. Validation and Discussion of Model Assumptions

The axial fuel regression model idealizes and neglects several effects: such as mutual diffusion time of oxygen-fuel mixture gas, buoyancy, and curvature effect. This section validates and discusses these idealized effects on model calculations.

5.4.1. Mixing Layer Thickness

Mixing layer thickness is schematically described as δ_m in Fig. 5.4. The model assumes the mixing time does not affect significantly on the heat input $\dot{q}_{in}$ calculation since the mixing layer thickness is smaller than the stand-off distance. However, it is a known fact that the concentration gradient at the flame leading edge: mixing layer thickness, affects the burning velocity [56]. Therefore, it is necessary to confirm that the mixing layer in stabilized combustion with liquid oxygen is thin enough not to affect burning velocity significantly. Hirota et al. experimentally revealed that the flame curvature at triple-flame edge has a directly proportional relationship with the concentration gradient at the flame edge, and the burning velocity gradually increases with increasing the flame curvature [48]. Kim et al. explained that thermal feedback from both side flame branches and the decrement of local gas velocity caused by thermal expansion makes the burning velocity higher than one-dimensional adiabatic laminar burning velocity [57]. On the other hand, Hirota et al. also showed the burning velocity has a peak at the flame curvature of 250 m^{-1} and conversely decreases with increasing the flame curvature; eventually, the velocity approaches the adiabatic laminar burning velocity again when flame curvature exceeds 1000 m^{-1}. They suggest a flame stretch effect exceeds the opposite effects referred in above at a specific concentration gradient, which makes burning velocity decrease with increasing flame curvature. Those previous research results suggest that the burning velocity perturbation by concentration gradient would be negligibly small in sufficiently large flame curvature such as flame edge not having a tribrachical structure. Linan et al. suggested the flame edge structure transform from triple-flame to edge-flame when the curvature radius δ_m/β is comparable or smaller than the flame-front thickness δ_L [58]; i.e. when the radius is comparable or smaller than stand-off distance δ, where β is Zeldovich number. This section inferred the flame edge structure in stabilized combustion from the local Damkohler number $(\delta_m/\beta\delta)^2$, which is a curvature radius to stand-off distance ratio, to confirm the validity of the assumption.

Since the previous section have already estimated flame front thickness as stand-off distance δ, the estimation of local Damkholer number $(\delta_m/\beta\delta)$ need the value of Zeldovich number β and calculate the mixing layer thickness δ_m. The definition of Zeldovich number β is the following;

$$\beta = \frac{E_a}{R_u T_b}\frac{T_b - T_g}{T_b} \quad (5.19)$$

where E_a is activation energy. Using 88.94 kJ/mol of the activation energy in oxygen and PMMA combustion from Ref. [59], the calculation results in $\beta \simeq 3$. Mixing layer thickness δ_m depends on species diffusion rate and mixture gas flow velocity. The increasing rate of the mixing layer thickness dy can be defined as the following equation using concentration gradient with the oxidizer-fuel gas binary diffusion coefficient D_{oxf}.

$$\frac{dy}{2} = -D_{oxf}\frac{d[\chi]}{dy}dt \approx \frac{D_{oxf}}{y}\frac{dx}{u_g} \quad (5.20)$$

$[\chi]$ is oxidizer or fuel gas mole fraction and dx is a distance where mixture gas flow in a time dt. Assuming mixture gas flow velocity u_g does not change along flow stram line, the integration of Eq. 5.20 from fuel surface to flame leading edge leads to the mixing layer thickness at the flame leading edge δ_m. as shown in Eq. 5.21.

$$\int_0^{\delta_m}\frac{y}{2}dy = \int_0^{\delta}\frac{D_{oxf}}{u_g}dx \quad \Rightarrow \quad \delta_m = 2\sqrt{\frac{D_{oxf}\delta}{u_g}} \quad (5.21)$$

Utilizing the Chapman-Enskog method can estimate a binary diffusion coefficient of oxidizer-fuel gas. Ref. [60] provides the modified formula for estimating binary diffusion coefficient as the following:

$$D_{oxf} = \frac{0.0266{T_{ig}}^{3/2}}{P_c MW_{oxf}{\sigma_{oxf}}^2\Omega_D} \quad (5.22)$$

This study uses an ignition temperature T_{ig} as a binary gas temperature. The other parameters are defined below:

$$MW_{oxf} = 2\left[1/MW_{ox} + 1/MW_f\right]^{-1} \quad (5.23)$$

where MW_{ox} and MW_f are the molecular weight of oxidizer and fuel gas, respectively;

$$\sigma_{oxf} = (\sigma_{ox} + \sigma_f)/2 \quad (5.24)$$

where σ_{ox} [Å] and σ_f [Å] are the hard-sphere collision diameters of oxidizer and fuel gas, respectively. The collision integral Ω_D is a dimensionless value calculated from the following expression;

$$\Omega_D = \frac{A}{(T^*)^B} + \frac{C}{\exp(DT^*)} + \frac{E}{\exp(FT^*)} + \frac{G}{\exp(HT^*)} \quad (5.25)$$

where A=1.06036, B=0.15610, C=0.19300, D=0.47635, E=1.03587, F=1.52996, G=1.76474, and H=3.89411. T^* is a dimensionless temperature calculated from the following equation;

$$T^* = T_{ig}\left(\frac{\epsilon_{ox}}{k_B}\frac{\epsilon_f}{k_B}\right)^{-1/2} \quad (5.26)$$

where k_B is the Boltzman constant [K], and ϵ_{ox} and ϵ_f are the characteristic Lennard-Jones energy of oxidizer and fuel gas, respectively. Parameters unique to oxidizer and fuel species: σ_{ox}, σ_f, ϵ_{ox}/k_B, and ϵ_f/k_B, use the values listed in Refs [61,62]; however, the parameters of fuel use that of ethyl acetate instead of MMA. Used parameters are listed in Table 5.4.

Table 5.4 Parameters list for estimation of mixing layer thickness and radius of flame curvature.

Parameter	Symbol	Value	Unit	Ref.
Oxidizer molecular weight	MW_{ox}	32.0	–	–
Fuel molecular weight	MW_f	100.12	–	–
Oxidizer hard-sphere collision diameter	σ_{ox}	3.467	Å	[61]
Fuel hard-sphere collision diameter	σ_f	5.205	Å	[62]
Oxidizer characteristic Lennard-Jones energy	ϵ_{ox}/k_B	106.7	K	[61]
Fuel characteristic Lennard-Jones energy	ϵ_f/k_B	521.3	K	[62]
Activation energy for combustion	E_a	88.94	kJ/mol	[59]

Figures 5.17 and 5.18 are the mixing layer thickness estimated under atmospheric and pressurized conditions, respectively. Figure 5.17 tells that the mixing layer thickness is approximately 0.8 mm and does not depend on oxidizer port velocity and port diameter because the term of stand-off distance δ and mixture gas velocity u_g in Eq. 5.21 offset both dependences each other. Figure 5.18 tells that the mixing layer thickness becomes thin with increasing chamber pressure due to the pressure dependence of binary diffusion coefficients. Figures 5.19 and 5.20 show each dependence on local Damkohler number with experimental results. Because the local Damkohler numbers are less than unity, these figures suggest that most of the stabilized combustion with liquid oxygen can neglect the mixing layer thickness effect on burning velocity except for high oxidizer port velocity and low pressure conditions. From the result shown in Fig. 5.19, though the model should consider the effect of mixing layer thickness on burning velocity perturbation under specific conditions, numerical simulation instead of an analytical model is necessary to accurately take burning velocity perturbation by concentration gradient change into fuel regression estimation.

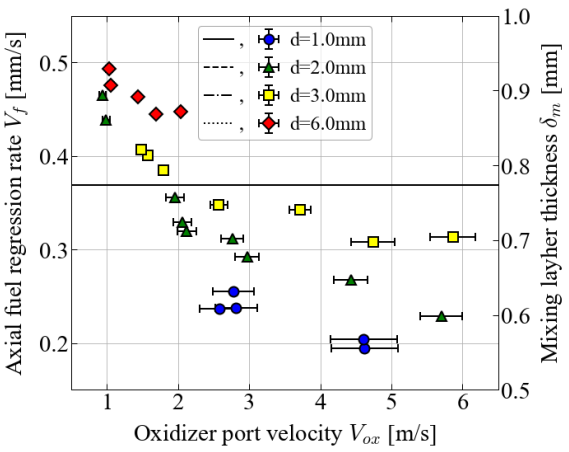

Fig.5.17 Mixing layer thickness under atmospheric conditions.

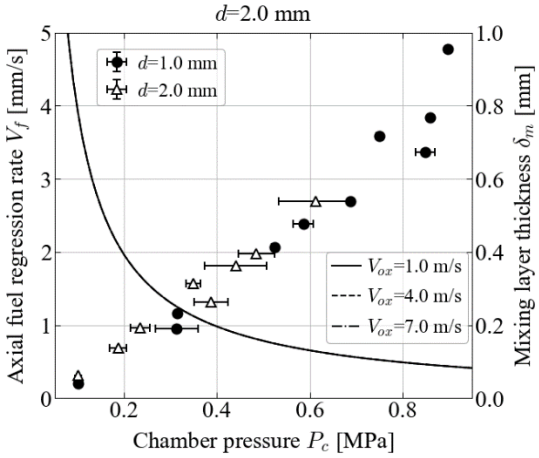

Fig.5.18 Pressure dependence on mixing layer thickness.

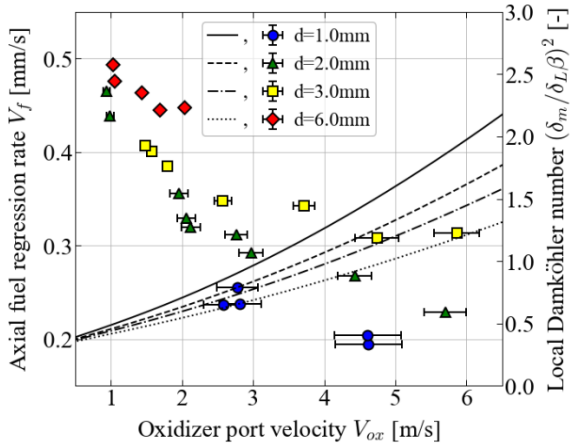

Fig.5.19 Oxidizer port velocity and port diameter dependence on local Damkohler number.

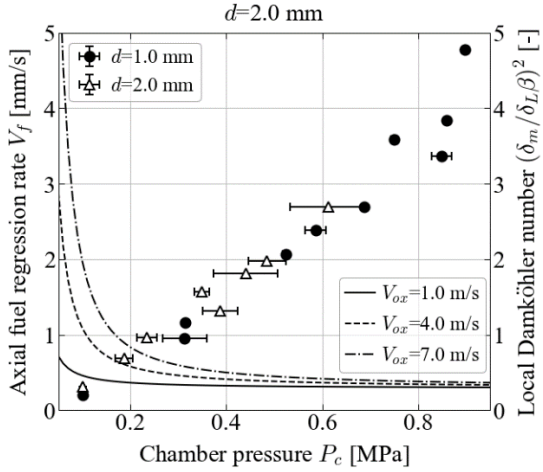

Fig.5.20 Pressure dependence on local Damkohler number.

5.4.2. Buoyancy Effect

Since the experiments with liquid oxygen and the actual use of AIEB hybrid rockets make diffusion flame spread upward against gravity, buoyancy should push back the mixture gas flowing into diffusion flame tip. However, the model does not consider the buoyancy effect that forces the flame edge to approach fuel surfaces, assuming the effect is negligibly minor than the inertia force of mixture gas. This section confirms that the buoyancy effect is small enough not to affect the heat input estimation significantly. The author used Richardson number Ri as an index for evaluating the buoyancy effect against inertia force. Assign the characteristic length as a mixing layer thickness δ_m, Ri number can be calculated the following equation;

$$Ri = \frac{g\alpha(T_b - T_g)\delta_m}{{u_g}^2} \quad (5.27)$$

where g is the gravitational acceleration (= 9.8 m/s^2) and α is volumetric thermal expansion coefficient. The linear approximation leads to the thermal expansion coefficient α as a temperature-dependent function, as shown below:

$$\alpha = -\frac{1}{\rho_g}\frac{\partial \rho_g}{\partial T} \approx \frac{T_b + T_g}{2T_bT_g} \quad (5.28)$$

Finally, the Richardson number Ri can be calculated by the following equation:

$$Ri = \frac{g\delta_m(T_b - T_g)}{{u_g}^2}\frac{T_b - T_g}{2T_bT_g} \quad (5.29)$$

Figures 5.21 and 5.22 show the calculated results of each dependence on the Richardson number. As shown in Fig. 5.21, the buoyancy effect becomes large with increasing oxidizer port velocity because the mixture gas velocity decrease, as stated in Sec 5.3.2. As shown in Fig. 5.22, the buoyancy effect rapidly becomes small with increasing chamber pressure because the mixing layer drastically becomes thin, as explained in the previous section. Generally, the buoyancy effect can be neglect when the order of Richardson number is comparable or less than 10^{-1}; however, the threshold value depends on the situation. Accordingly, these results suggest that the model can neglect the buoyancy effect when chamber pressure is higher than 2.0 MPa; even when atmospheric pressure conditions, the effect is minor compared with inertia force. These results also suggest taking the buoyancy effect into the model will improve the oxidizer port diameter sensitivity of fuel regression rate under atmospheric

conditions. This is because the effect gradually becomes large with increasing oxidizer port velocity, leading to the increasing heat input to fuel surfaces.

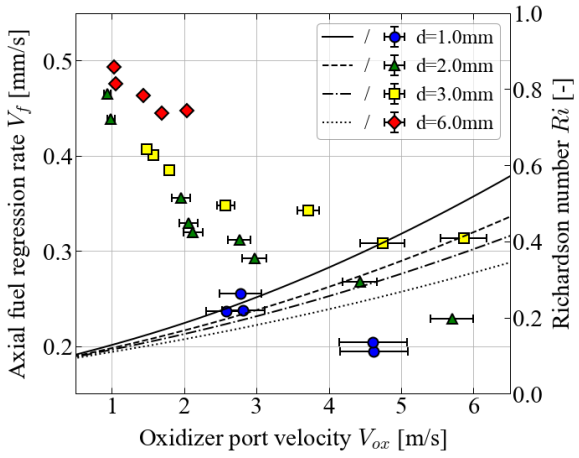

Fig.5.21 Oxidizer port velocity and port diameter dependence on Richardson number under atmospheric conditions.

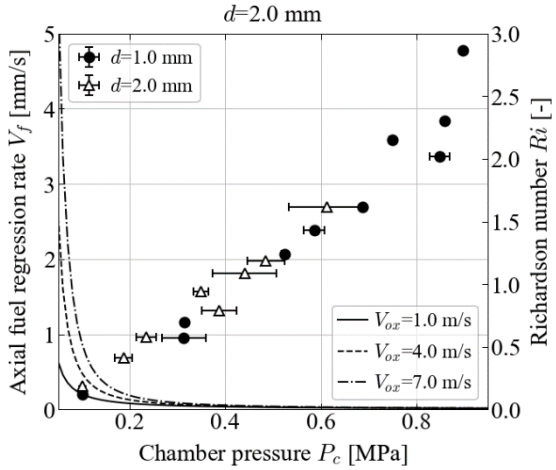

Fig.5.22 Pressure dependence on Richardson number when d=2.0 mm and several oxidizer port velocity conditions.

5.4.3. Curvature Effect

The model assumes flame spreading in parallel flat plates for simplification; however, this study focuses and experimentally investigates the flame spreading into a circular fuel duct. The discussion of port diameter dependence on axial fuel regression rate should consider the curvature effect, particularly when port diameter becomes small and comparable to the control volume size. Two mechanisms cause the curvature effect: the discrepancies between heat input area S_{in} and heat loss area S_{cool} of a control volume, and effective area of diffusion flame tip S_b.

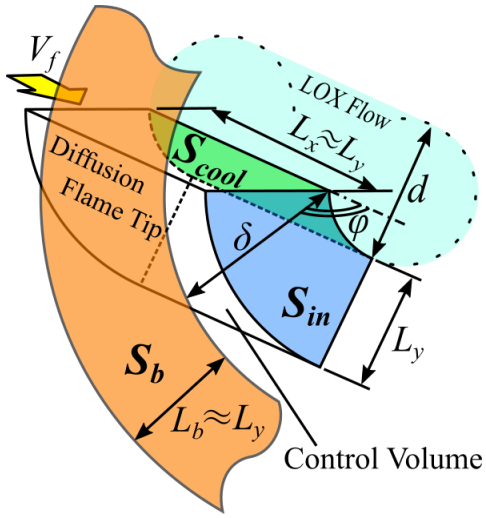

Fig.5.23 Difference between each surface area where heat transfers occur causes curvature effect.

Figure 5.23 schematically shows the differences between each surface causing curvature effects. L_x is a thermal penetration depth: i.e., control volume length for axial direction, L_y is a conrtrol volume thickness, L_b is an effective thickness of diffusion flame tip, and ϕ is an inclination angle of flame tip location consisting of the port axis and stoichiometric line. Although the model assumes these three surfaces have the same area, heat loss area S_{cool} becomes smaller, and effective area of diffusion flame tip S_b becomes larger than heat input area S_{in} considering curvature effect. Since it is difficult for this study to estimate and formulate each length: L_x, L_y, and L_b, as a pressure, oxidizer velocity, or port diameter function, this section assumes they have the same length, as the same manner in the model constructed in Sec. 5.1. Assuming the inclination angle ϕ is 45°, the effective area of the flame tip S_b is calculated by the following equation:

$$\begin{aligned} S_b &= \pi\left(\frac{d}{2} + \delta sin\phi + L_b\right)^2 - \pi\left(\frac{d}{2} + \delta sin\phi\right)^2 \\ &\approx \pi L_y(d + 2\delta sin\phi + L_b) \end{aligned} \qquad (5.30)$$

Also, the heat input area S_{in} and the heat loss area S_{cool} are calculated by the following equations:

$$S_{in} = \pi\left(\frac{d}{2} + L_y\right)^2 - \pi\left(\frac{d}{2}\right)^2 = \pi L_y\left(d + L_y\right) \quad (5.31)$$

$$S_{cool} = \pi L_x d \approx \pi L_y d \quad (5.32)$$

The energy conservation equation is derived by adding each area ratio to heat flux terms as curvature effect correction factors and yields the analytical solution of axial fuel regression rate as the following:

$$\dot{q}_{net} = \frac{S_b}{S_{in}}\dot{q}_{in} - \frac{S_{cool}}{S_{in}}\dot{q}_{cool} \quad (5.33)$$

$$V_f = \frac{1}{2Q_{net}}\left(\sqrt{\frac{S_{cool}}{S_{in}}\dot{q}_{cool} + 4\frac{S_b}{S_{in}}Q_{net}Q_{in}} - \frac{S_{cool}}{S_{in}}\dot{q}_{cool}\right) \quad (5.34)$$

Figures 5.24 and 5.25 show the port diameter dependence on each area ratio varying control volume thickness from 0.1 to 0.6 mm under atmospheric conditions when oxidizer port velocity is 2.0 m/s and 6.0 m/s, respectively. These figures explain the port diameter trends of each curvature effect caused by two mechanisms: smaller heat loss area S_{cool} and larger effective flame tip area S_b. Both cases indicate that the curvature effect becomes significant in small port diameter. Focusing on each area ratio, heat input increases, and heat loss decreases as the port diameter becomes small, resulting in an axial fuel regression rate increasing with decreasing port diameter. For example, a thermal penetration depth L_x becomes small as axial fuel regression rate increase, which will lead to large S_{cool}/S_{in} in small port diameter. Therefore, it is necessary to consider the variation of control volume aspect ratio into model construction in future work.

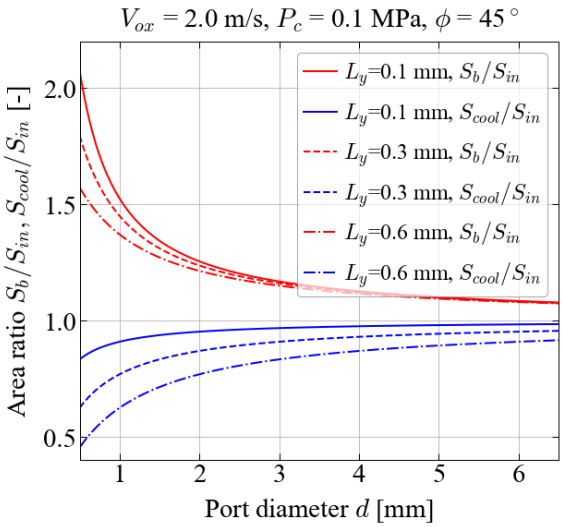

Fig.5.24 Port diameter dependence on area ratios under atmospheric pressure when V_{ox}=2.0 m/s and ϕ=45°.

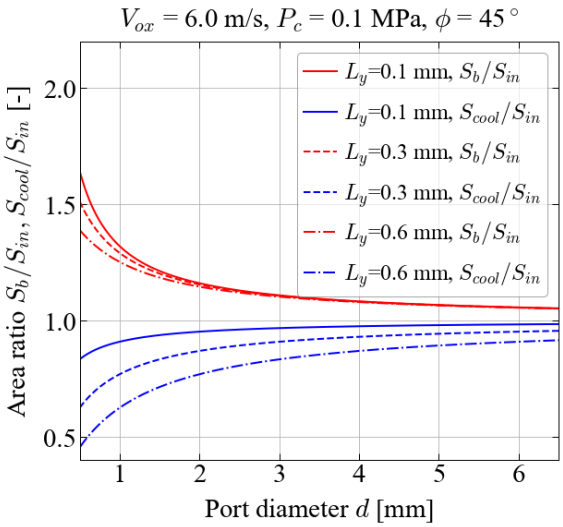

Fig.5.25 Port diameter dependence on area ratios under atmospheric pressure when V_{ox}=6.0 m/s and ϕ=45°.

Figures 5.26 and 5.27 show the comparison between the results calculated by the no-curvature effect model: Eq. 5.14, and the model considering curvature effect: Eq. 5.34. Also, experimental results calculated by the empirical formula: Eq. 4.1, are shown in both figures. The calculating condition of Figs 5.26 and 5.27 are the same in that of Figs 5.24 and 5.25, respectively. The model results considering the curvature effect show the opposite trend to the experiment and no-curvature effect model in the port diameter dependence on the axial fuel regression rate in both figures. This is because, as stated above section, heat input increases heat loss decreases as the port diameter becomes small when considering the curvature effect. For the same reason, the fuel regression rate in thicker control volume conditions becomes slightly higher than when the control volume thickness L_y is thin. Since the analysis in the curvature effect shows the opposite trend to the real phenomena in port diameter dependence on axial fuel regression rate, these results suggest that other factors might have a significant effect on port diameter dependence. One possible reason is the variation of the control volume aspect ratio. The model constructed above, including the model considering curvature effect, assumes that thermal penetration depth L_x and control volume thickness L_y have the same length; however, these lengths should be affected by fuel regression rate and fuel regression shape.

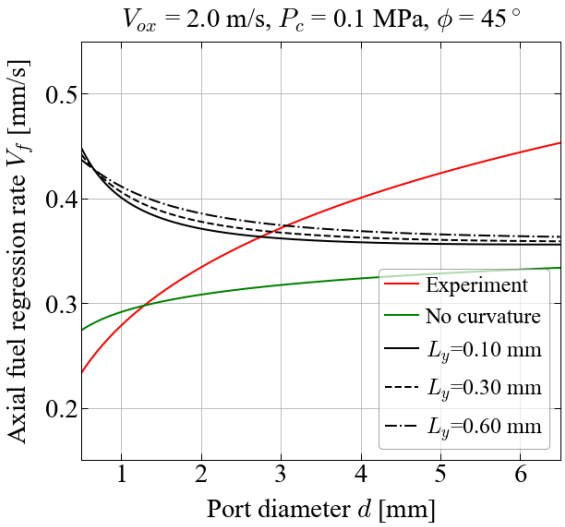

Fig.5.26 Curvature effect on axial fuel regression rate comparing under atmospheric pressure when V_{ox}=2.0 m/s and ϕ=45°.

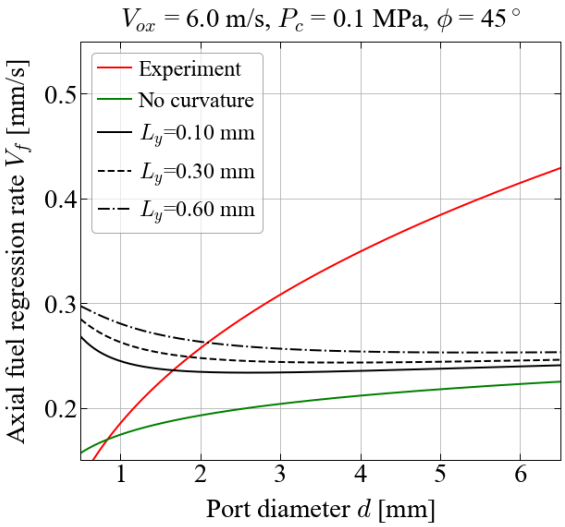

Fig.5.27 Curvature effect on axial fuel regression rate comparing under atmospheric pressure when V_{ox}=6.0 m/s and ϕ=45°.

5.4.4. Wall Temperature Variation

The model assumes port wall temperature constant even though the oxidizer port velocity and port diameter conditions are changed because of temperature measurement's difficulty. However, many factors such as oxidizer port velocity, port diameter, and fuel regression rate would affect the wall temperature. This section discusses the effect of port wall temperature variation on axial fuel regression rate, estimating wall temperature from the empirical formula and constructed model. Substituting the axial fuel regression rate calculated by the empirical formula to the fuel regression model, the average wall temperature $\bar{T}_w$ can be estimated backward from Eq. 5.14. Figure 5.28 shows the estimated average wall temperature under atmospheric pressure varying oxidizer port velocity and port diameter conditions. This figure indicates the port wall temperature in smaller port diameter is higher than in larger port diameter, which means that heat transfer becomes active as the port diameter is small. These results are reasonable because the curvature effects make the amount of heat input relatively large than heat loss as the port diameter becomes small, as shown in Figs. 5.24 and 5.25. Oxidizer port velocity does not significantly affect port wall temperature except for low port velocity. In higher oxidizer port velocity than around 3 m/s, wall temperature gradually decrease with increasing oxidizer port velocity because the high oxidizer flow rate intensifies the heat transfer from the port wall to liquid oxygen. On the other hand, the results also suggest that the heat transfer mode changes from turbulent heat transfer to boiling heat transfer or other high rate heat transfer mode at around 2.0 m/s of oxidizer port velocity because low mass flow rate causes subcooled boiling or surface boiling.

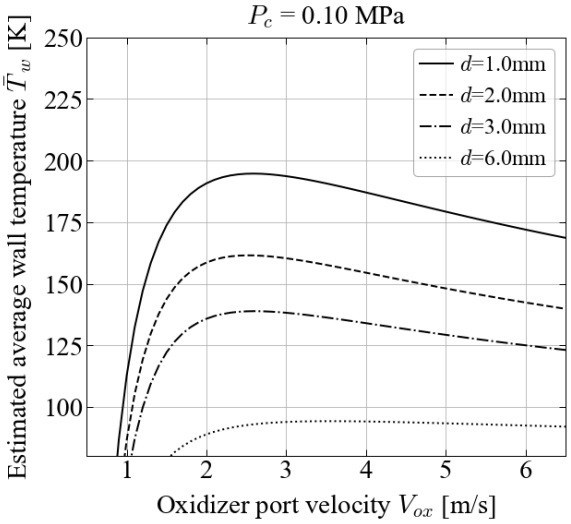

Fig.5.28 Estimated average wall temperatures are different from port diameter conditions.

Figures 5.29 and 5.30 show the experimental results and the calculation results when the port diameter is 2.0 and 3.0 mm, respectively; in calculations, the port wall temperature varies from 120 to 210 K under the atmospheric pressure. As suggested in Fig 5.28, Fig 5.29 and 5.30 tell that slightly lower temperatures: around 150 K when d=2.0 mm and 120 K when d=3.0 mm, show better agreements with experimental results than 180 K of average wall temperature used in previous discussion and analysis. Also, these figures suggest the wall temperature decreasing gradually with increasing oxidizer port velocity would show better agreements with experimental results than that of the constant wall temperature model.

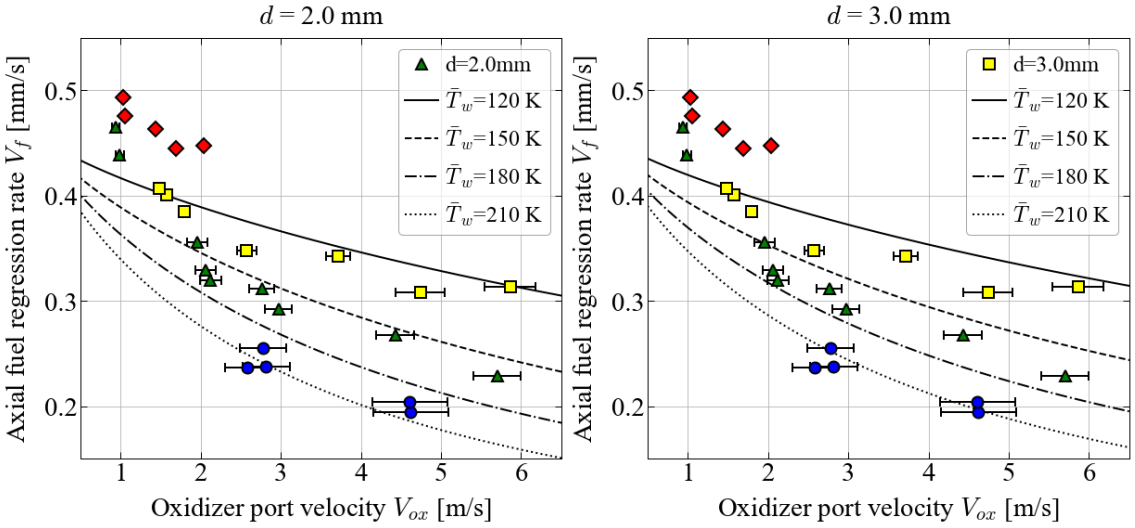

Fig.5.29 Port wall temperature dependence on axial fuel regression rate under atmospheric pressure when d=2.0 mm.

Fig.5.30 Port wall temperature dependence on axial fuel regression rate under atmospheric pressure when d=3.0 mm.

CHAPTER 6.

FUEL REGRESSION SHAPE

Fuel regression shape at the port exit is the second most critical characteristic of AIEB hybrid rockets after axial fuel regression rate. Figure 6.1 is the schematic of the transition to end-burning mode in AIEB hybrid rocket fuels. As shown in the figure, AIEB hybrid rocket fuels achieve an end-burning mode when the diffusion flame at each port exit enlarging the port diameters until ports merge with one other. Therefore, if the pitch between ports is wide, it takes a long time to achieve an end-burning mode after ignition. In the worst case, diffusion flames may reach the fuel front end surface before the ports merge, and an end-burning mode is never achieved [8]. To assign an appropriate port diameter and port pitch in the multi-port fuel design for AIEB hybrid rockets, it is necessary to investigate the characteristics of fuel regression shape at the port exit with liquid oxygen. This research focused on the dependence of the fuel regression shape on port diameter, oxidizer port velocity, and chamber pressure.

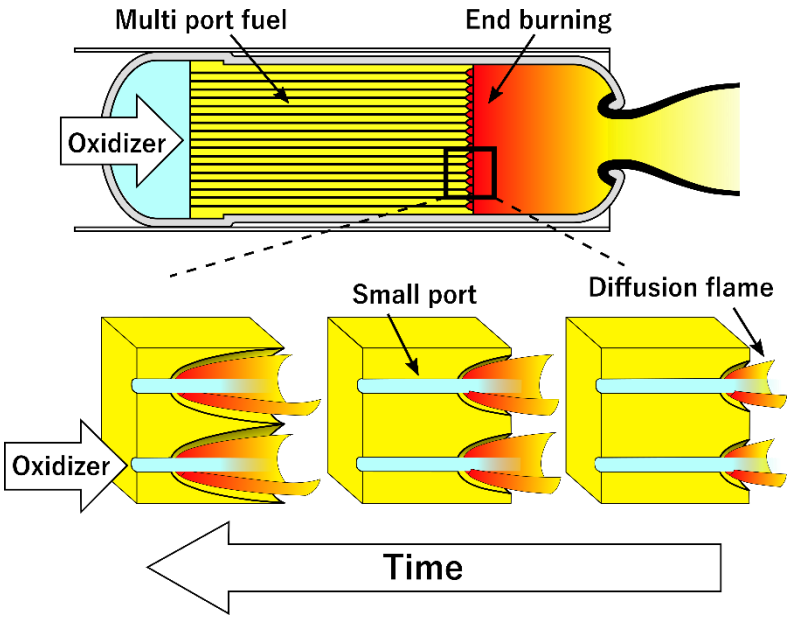

Fig.6.1 Transition to an end-burning mode in axial-injection end-burning hybrid rocket fuel.

Figure 6.2 shows an example image of a fuel sample after a firing test captured by a scanner. This study obtained radial fuel regression distance concerning axial distance from the scanned image, as shown in Fig. 6.2, and revealed the relations to the experimental conditions to investigate the regression shape characteristic. Image processing software was used to manually extract the point cloud coordinates on the regressed surface from the scanned image as the regression shape. Assuming the regression shape is axisymmetric, the analysis used the averaged data from both sides of the regression distance.

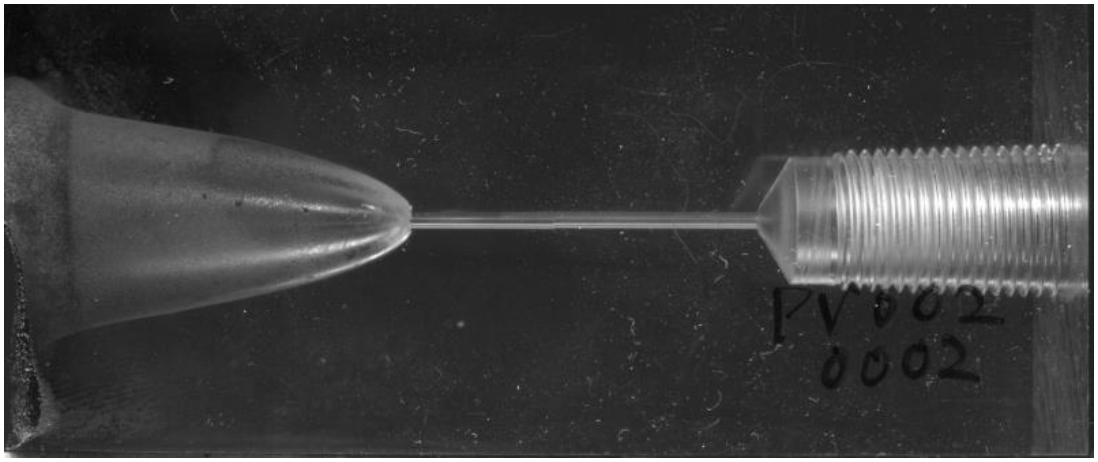

Fig.6.2 An example picture of a fuel sample after firing, captured by scanner.

6.1. Effect of Port Diameter, Oxidizer Port Velocity, and Chamber Pressure

The analysis used the fuel regression data obtained from the fuel samples used to investigate the axial fuel regression rate and organized these data in terms of port diameter, oxidizer port velocity, and chamber pressure. Figures 6.3, 6.4, and 6.5 show the regression shape under atmospheric pressure when the port diameter is 1.0, 2.0, 3.0 mm, respectively. The horizontal axis is axial distance x from the enlarged duct tip, and the vertical axis is radial regression distance y from the virgin port wall surface. Note that the radial regression distance is not the distance from the center of a port. Each figure organized for port diameter shows that the regression shape slightly tends to become wide with increasing oxidizer port velocity. Concerning port diameter, the regression shape also slightly tends to widen with decreasing port diameter. However, this data is insufficient to conclude that both tendencies have a clear correlation. On the other hand, Fig. 6.6, which is organized for chamber pressure when the port diameter is 2.0 mm and oxidizer port velocity around 3.0 m/s, shows a clear

correlation with the regression shape and chamber pressure, such that the shape becomes more acute with increasing chamber pressure.

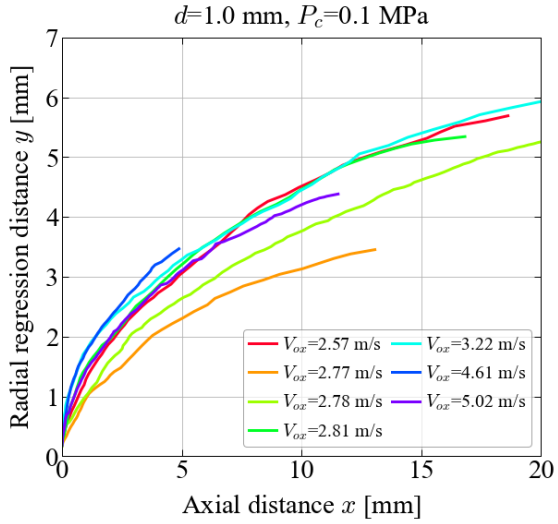

Fig.6.3 Fuel regression shape under atmospheric pressure condition when port diameter, d, is 1.0 mm.

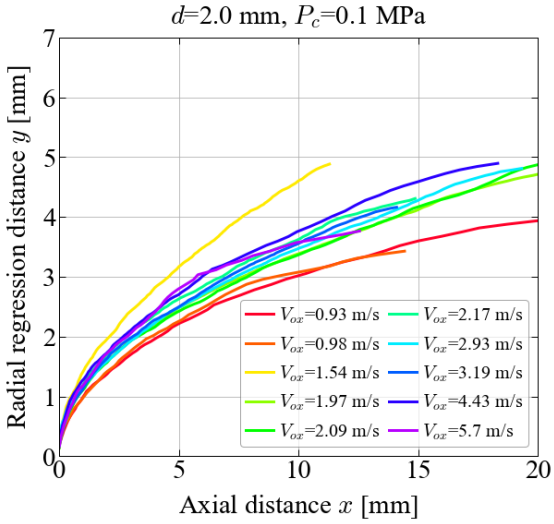

Fig.6.4 Fuel regression shape under atmospheric pressure condition when port diameter, d, is 2.0 mm.

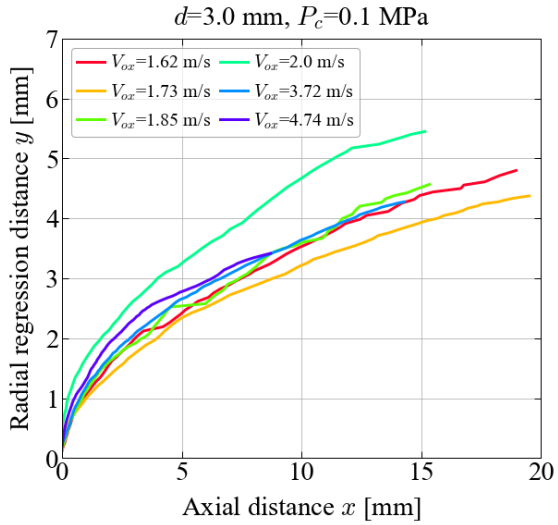

Fig.6.5 Fuel regression shape under atmospheric pressure condition when port diameter, d, is 3.0 mm.

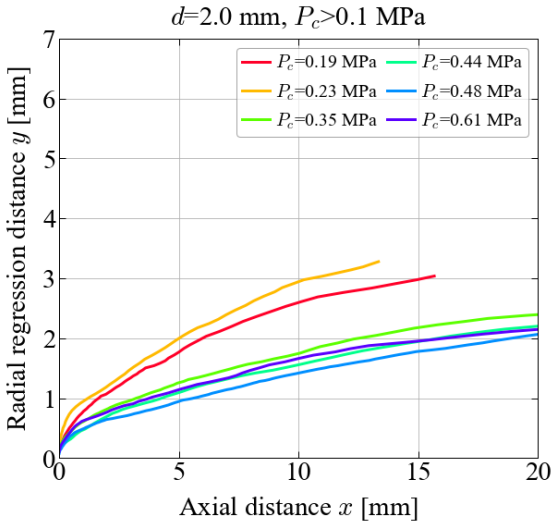

Fig.6.6 Fuel regression shape under several ambient pressure levels when port diameter, d, is 2.0 mm.

6.2. Radial Fuel Regression Rate

Radial fuel regression can be calculated from the measurements of fuel regression shape. Figure 6.7 shows the relations between radial fuel regression rate, $\dot{r}$, and axial fuel regression rate, V_f.

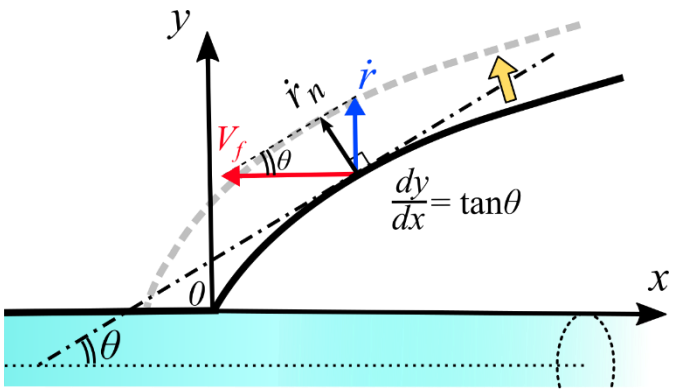

Fig.6.7 Relationship between radial regression rate, $\dot{r}$, and axial regression rate, V_f.

Note that both axial fuel regression rate V_f and radial fuel regression rate $\dot{r}$ are apparent velocities in axial and radial direction because the regression rate normal to regression surface $\dot{r}_n$ is the actual fuel regression rate. Defining the angle θ between the port axis and the tangent line of the regression surface, when the shape is a steady-state, the radial fuel regression rate $\dot{r}$ can be calculated from Eq. 6.1 using the axial fuel regression rate V_f.

$$\dot{r} = V_f tan\theta = V_f \frac{dy}{dx} \qquad (6.1)$$

The axial derivative of regression distance used the 4th order central difference scheme to suppress the data fluctuation. Figures 6.8, 6.9, and 6.10 show the radial fuel regression rate under atmospheric pressure determined from Eq. 6.1 when the port diameter is 1.0, 2.0, and 3.0 mm, respectively. These figures indicate that the radial fuel regression rate around an enlarged duct tip is the highest, and the regression rate decreases in the downstream direction. This is because the laminar boundary layer thickness becomes thick, and the gaseous mass flux decreases due to the enlarging of the regressed duct area. Previous research investigating a conventional hybrid rocket reported similar axial distribution in port regression rate [63]. It seems that port diameter slightly affects the radial fuel regression rate, and the regression rate tends to be low when the port diameter is small. However, in the downstream region, the regression rate is independent of the port diameter. On the other hand,

oxidizer port velocity barely affects the radial fuel regression rate. All atmospheric pressure results revealed that the averaged radial fuel regression rate was around 0.1 mm/s, approximately a fifth to a third of a conventional hybrid rocket employing tubular fuel [64]. Figure 6.11 shows axial distribution of the radial fuel regression rate with various chamber pressure. The figure indicates that the regression rate tends to be high in high chamber pressure conditions. High pressure conditions make the tip of diffusion flame approach to fuel surfaces as stated in Sec. 5.3.1., which increases the gasified fuel and oxygen mass flow rate. Also, high pressure conditions make the cross-sectional area of regression shape decrease as described in Fig. 6.6. Accordingly, the high gaseous mass flux in high chamber pressure conditions promotes radial fuel regression rate in the same manner as conventional hybrid rockets employing a tubular type fuel.

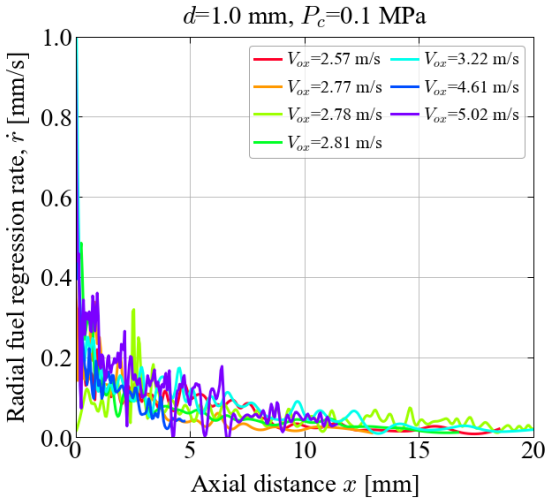

Fig.6.8 Axial distribution of radial fuel regression rate under atmospheric pressure condition when port diameter, d, is 1.0 mm.

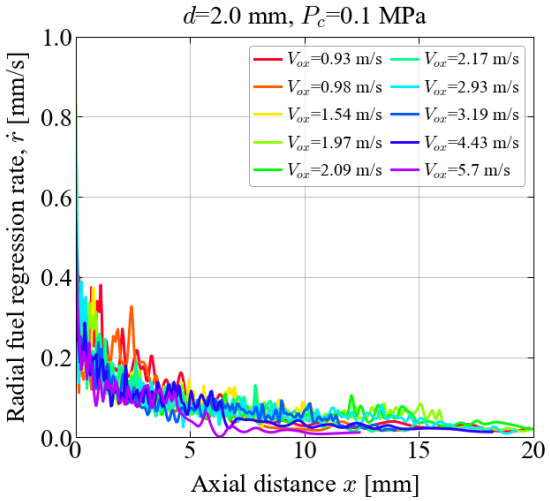

Fig.6.9 Axial distribution of radial fuel regression rate under atmospheric pressure condition when port diameter, d, is 2.0 mm.

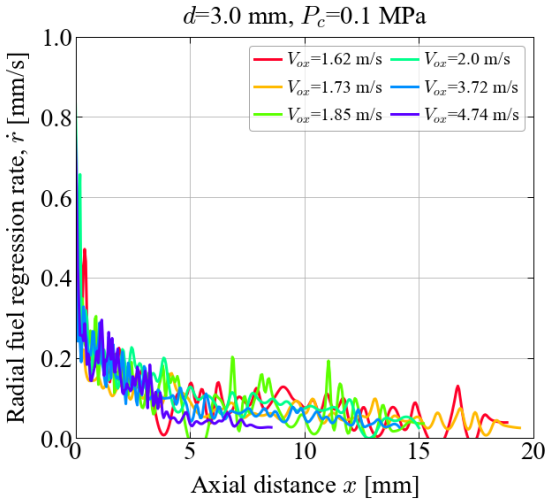

Fig.6.10 Axial distribution of radial fuel regression rate under atmospheric pressure condition when port diameter, d, is 3.0 mm.

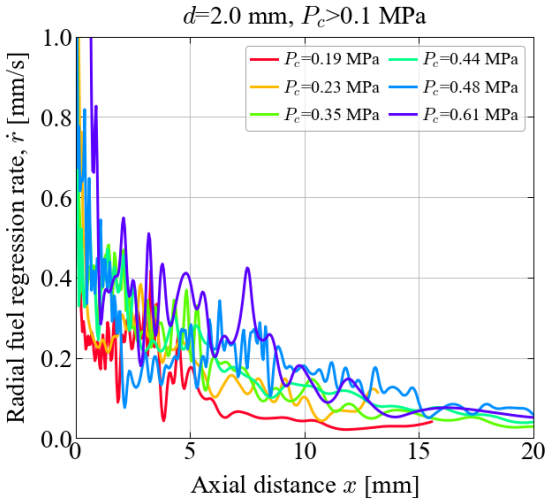

Fig.6.11 Axial distribution of radial fuel regression rate under several ambient pressure levels when port diameter, d, is 2.0 mm.

6.3. Constructing Empirical Formula of Regression Shape

The experimental results revealed that the regression shape tends to be slightly more obtuse with increasing oxidizer port velocity and decreasing port diameter, and significantly more acute with increasing chamber pressure. These tendencies are the same as the correlation between axial fuel regression and the experimental conditions; namely, the results suggest that the regression shape becomes more acute when the axial fuel regression rate is high. From this point of view, this section constructed the empirical formula of regression shape as a function of axial fuel regression rate, assuming the regression rate rules the regression shape. The empirical formula introduced two principal parameters of α and β, which represent the feature of regression shape. Though the regression shape formed by stabilized combustion is like a bell-shape, the regression distance should not be infinitely large further downstream, like a parabola, and close to a certain regression distance when the diffusion flame runs out of the supplied liquid oxygen. One of the quantities introduced α represents the maximum regression distance when the axial distance is infinite and the other quantity β represents the ease of closing to the maximum regression distance α. Considering the definition of these two parameters of α and β, the empirical formula of regression shape is defined as the following:

$$y = \alpha\left[1 - \exp\left(-x^{\beta}\right)\right] \qquad (6.2)$$

where the unit of regression distance y and axial distance x are [m], and the range of β is (0. 1). Both parameters of α and β must be functions of the axial fuel regression rate V_f. Figures 6.12 and 6.13 show the dependences of α and β on the axial fuel regression rate, respectively.

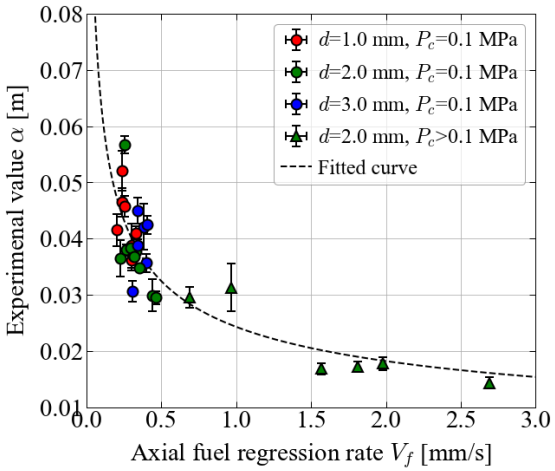

Fig.6.12 Relationship between axial fuel regression rate, V_f, and empirical constant, α.

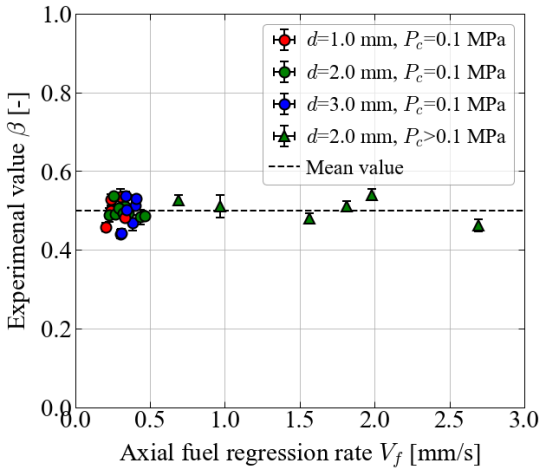

Fig.6.13 Relationship between axial fuel regression rate, V_f, and empirical constant, β.

These figures indicate that the maximum regression distance, α, decreases exponentially with the increasing axial fuel regression rate. On the other hand, β is almost not affected by the axial fuel regression rate and is a constant value. Performing a regression analysis using Eq. 6.3 as a regression curve, the analysis results in the two empirical values, k_1 and k_2. The value of β for the empirical formula is identified as averaged constant.

$$\alpha = k_1 {V_f}^{k_2} \qquad (6.3)$$

where the unit of axial fuel regression rate, V_f, is [m/s], and that of maximum regression distance, α, is [m/s]. Table 6.1 shows the obtained empirical constants and their standard error. For evaluating the accuracy of the constructed empirical formula, the following two figures show comparisons with experiments. Figure 6.14 shows the absolute error from the experimentally obtained regression distance. Figure 6.15 shows the relative error from the experimentally obtained regression distance.

Table 6.1 List of empirical constants related to fuel regression shape.

Empirical constant	Value	Standard error
k_1	1.36×10^{-3}	0.67×10^{-3}
k_2	-0.417	0.061
$\bar{\beta}$	0.500	0.028

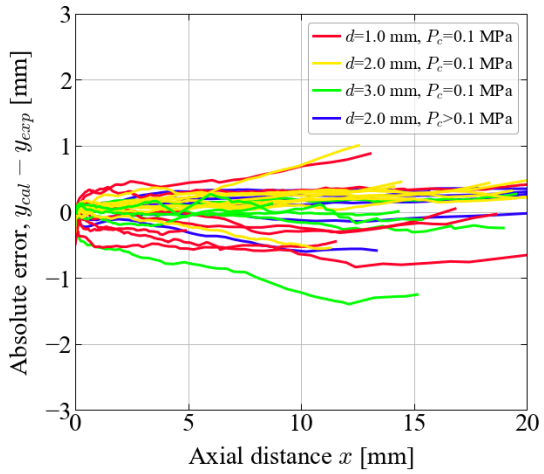

Fig.6.14 Absolute error between calculated regression shape and experiment.

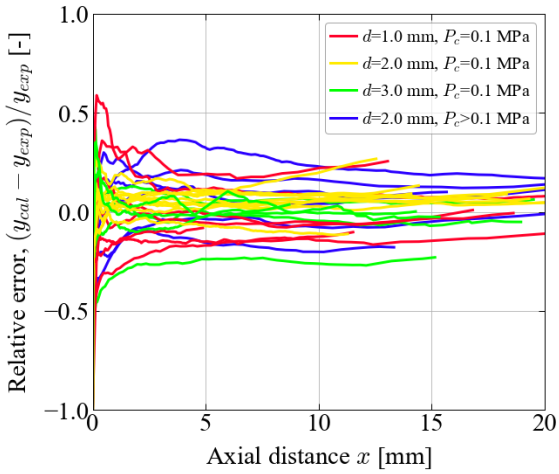

Fig.6.15 Relative error between calculated regression shape and experiment.

These figures indicate that each error's axial distribution does not have any specific bias, and the error size is within around ±1 mm in absolute error, $\pm25\%$ in relative error. Because the variation of experimental condition will make a larger difference than the error; e.g., the difference will be up to 4 mm at x=20 mm when the chamber pressure difference is 0.5 MPa, the constructed empirical formula agrees qualitatively with the experimental result and is accurate enough to estimate the shape for designing multiport fuel.

CHAPTER 7.

CONCLUDING REMARKS

This research experimentally investigated the fuel regression characteristics of stabilized combustion when liquid oxygen is supplied to a fuel duct. The experiments revealed that combustion with liquid oxygen could be classified as stabilized combustion because it has the same features as that of stabilized combustion as first proposed in experiments with gaseous oxygen. Extinction and abnormal regression were also reported when the oxidizer port velocity was high, and the port diameter was small. The observation of temperature distribution around the enlarged duct tip suggested that the significant cooling of a fuel port surface by liquid oxygen generates a skinny tube-shaped section of unburned fuel protected by the oxygen supply, which leads to extinction and abnormal regression.

The axial fuel regression rate is the most critical regression characteristic, and depends on port diameter, oxidizer port velocity, and chamber pressure. Experimental results showed that the regression rate is predominately a function of chamber pressure, but also increases slightly with decreasing oxidizer port velocity and increasing port diameter. Two of these dependences: oxidizer port velocity and chamber pressure, are the same as reported in the stabilized combustion with gaseous oxygen. On the other hand, the port diameter dependence on axial fuel regression rate was unique to liquid oxygen-based stabilized combustion. The empirical formula for axial fuel regression rate was constructed and evaluated for accuracy.

A physical model of the axial fuel regression rate was constructed considering the heat balance of heat input, heat loss, and net heat consumption in the enlarged fuel duct tip. The comparison between the model and the experiment showed that the model's calculated results agreed qualitatively with each tendency: port diameter, oxidizer port velocity, and chamber pressure dependence, which suggested the model's validity. Furthermore, the physical mechanisms causing each dependence were revealed utilizing this model, showing that extinction and abnormal regression occurs when heat loss exceeds around 1.4~1.6 MW/m^2. The discussion of the model's assumptions reveals that the mixing layer thickness and buoyancy effects do not significantly affect the axial fuel regression rate calculation; however, the model should consider wall temperature variation and curvature effects to

improve port diameter and oxidizer port velocity dependencies.

The fuel regression shape, which was obtained from fuel samples after firing tests, is the second most critical regression characteristic and was organized in terms of port diameter, oxidizer port velocity, and chamber pressure. The analysis indicated that chamber pressure significantly affects the regression shape. The empirical formula to predict the regression shape was also constructed as a function of the axial fuel regression rate, assuming that the axial fuel regression rate governs the regression shape. The comparison between the experiment and empirical formula suggests that because the error was around $\pm 25\%$ in relative error, the formula is accurate enough to estimate the shape qualitatively.

REFERENCE

[1] Satellite Industry Association, 2017 State of the Satellite Industry Report, Bryce Space and Technolog, 2017.

[2] A. Poghosyan, A. Golkar, CubeSat evolution: Analyzing CubeSat capabilities for conducting science missions, Prog. Aerosp. Sci. 88 (2017) 59–83. https://doi.org/10.1016/j.paerosci.2016.11.002.

[3] T. Wekerle, J.B.P. Filho, L.E.V.L. da Costa, L.G. Trabasso, Status and Trends of Smallsats and their Launch Vehicles — An Up-to-date Review, Journal of Aerospace Technology and Management. 9 (2017) 269–286. https://doi.org/10.5028/jatm.v9i3.853.

[4] D. Altman, A. Holzman, Overview and History of Hybrid Rocket Propulsion, in: J.M. Chiaverini, K.K. Kuo (Eds.), Fundamentals of Hybrid Rocket Combustion and Propulsion, 1st ed., American Institute of Aeronautics and Astronautics, Reston, Virginia, 2007.

[5] M.A. Hitt, R.A. Frederick, Survey of Previous and Recent Enhancements of Hybrid Rocket Motor Regression Rates, in: 53rd AIAA/SAE/ASEE Joint Propulsion Conference, American Institute of Aeronautics and Astronautics, Reston, Virginia, 2017. https://doi.org/10.2514/6.2017-4969.

[6] T. Inamoto, J. Okuyama, S. Murofushi, K. Miyagawa, A. Takada, Study on the Burning Property of a Solid Propellant Containing Ammonium Perchlorate Synthesized Using a New Method (in Japanese), Journal of IHI Technology. 51 (2011).

[7] H. Nagata, K. Okada, T. Sanda, T. Kato, R. Akiba, S. Satori, I. Kudo, Combustion Characteristics of Fibrous Fuels for Dry Towel Hybrid Rocket Motor, J. Space Technol. Sci. 13 (1997) 11–16. https://doi.org/10.11230/jsts.13.1_11.

[8] N. Hashimoto, End-burning type hybrid rocket, Ph.D dissertaion (in Japanese), Hokkaido University, Sapporo, Japan, 2004.

[9] H. Nagata, H. Teraki, Y. Saito, R. Kanai, H. Yasukochi, M. Wakita, T. Totani, Verification Firings of End-Burning Type Hybrid Rockets, J. Propul. Power. 33 (2017) 1473–1477. https://doi.org/10.2514/1.B36359.

[10] Y. Saito, Combustion Mechansms of Axial-Injection End-Burning Hybrid Rockets, Ph.D dissertaion (in Japanese), Ph.D., Hokkaido University, 2018.

https://doi.org/10.14943/doctoral.k13203.

[11] Y. Saito, T. Yokoi, L. Neumann, H. Yasukochi, K. Soeda, T. Totani, M. Wakita, H. Nagata, Investigation of axial-injection end-burning hybrid rocket motor regression, Advances in Aircraft and Spacecraft Science. 4 (2017) 281–296. https://doi.org/10.12989/aas.2017.4.3.281.

[12] Y. Saito, M. Kimino, A. Tsuji, Y. Okutani, K. Soeda, H. Nagata, High Pressure Fuel Regression Characteristics of Axial-Injection End-Burning Hybrid Rockets, J. Propul. Power. 35 (2019) 328–341. https://doi.org/10.2514/1.B37135.

[13] Y. Okutani, Y. Saito, M. Kimino, A. Tuji, K. Soeda, H. Nagata, Investigation of Regression Rate under High-Pressure in Axial-Injection End-Burning Hybrid Rockets, in: 2018 Joint Propulsion Conference, American Institute of Aeronautics and Astronautics, Reston, Virginia, 2018. https://doi.org/10.2514/6.2018-4529.

[14] Y. Saito, T. Yokoi, A. Tsuji, K. Omura, H. Yasukochi, K. Soeda, T. Totani, M. Wakita, H. Nagata, Investigation of the Throttling Characteristics of Axial-injection End-burning Hybrid Rockets (in Japanese), J. Jpn. Soc. Aeronaut. Space Sci. 65 (2017) 157–167.

[15] M.A. Hitt, R.A. Frederick, Experimental evaluation of a nitrous-oxide axial-injection, end-burning hybrid rocket, J. Propul. Power. 33 (2017) 1555–1560. https://doi.org/10.2514/1.B36439.

[16] R. Okuda, K. Komizu, A. Tsuji, T. Miwa, S. Yokobori, K. Soeda, L.T. Kamps, H. Nagata, Fuel Regression Characteristics of Axial-Injection End-Burning Hybrid Rocket Using Nitrous Oxide, in: AIAA Propulsion and Energy 2020 Forum, 2020: pp. 1–14. https://doi.org/10.2514/6.2020-3753.

[17] N. Hashimoto, S. Watanabe, H. Nagata, T. Totani, I. Kudo, Opposed-flow flame spread in a circular duct of a solid fuel: Influence of channel height on spread rate, Proc. Combust. Inst. 29 (2002) 245–250. https://doi.org/10.1016/S1540-7489(02)80033-5.

[18] N. Hashimoto, H. Nagata, T. Totani, I. Kudo, Determining factor for the blowoff limit of a flame spreading in an opposed turbulent flow, in a narrow solid-fuel duct, Combust. Flame. 147 (2006) 222–232. https://doi.org/10.1016/j.combustflame.2006.07.015.

[19] T. Matsuoka, S. Murakami, H. Nagata, Transition characteristics of combustion modes for flame spread in solid fuel tube, Combust. Flame. 159 (2012) 2466–2473. https://doi.org/10.1016/j.combustflame.2012.03.001.

[20] I.S. Wichman, Theory of opposed-flow flame spread, Prog. Energy Combust. Sci. 18 (1992) 553–593. https://doi.org/10.1016/0360-1285(92)90039-4.

[21] X. Huang, J. Gao, A Review of Near-Limit Fire Spread in Opposed Flow, Fire Safety Journal

[Invited Review]. (2020) 103141. https://doi.org/10.1016/j.firesaf.2020.103141.

[22] F.A. Williams, Mechanisms of fire spread, Symp. Combust. 16 (1977) 1281–1294. https://doi.org/10.1016/S0082-0784(77)80415-3.

[23] A.C. Fernandez-Pello, T. Hirano, Controlling Mechanisms of Flame Spread, Combust. Sci. Technol. 32 (1983) 1–31. https://doi.org/10.1080/00102208308923650.

[24] A. Ito, T. Kashiwagi, Temperature measurements in PMMA during downward flame spread in air using holographic interferometry, Symp. Combust. 21 (1988) 65–74. https://doi.org/10.1016/S0082-0784(88)80232-7.

[25] A. Ito, Y. Kudo, H. Oyama, Propagation and extinction mechanisms of opposed-flow flame spread over PMMA for different sample orientations, Combust. Flame. 142 (2005) 428–437. https://doi.org/10.1016/j.combustflame.2005.04.004.

[26] P. Stang, J. Steinz, M. Summerfield, The burning mechanism of ammonium perchlorate- based composite solidpropellants, in: 4th Propulsion Joint Specialist Conference, Princeton University, Reston, Virigina, 1968. https://doi.org/10.2514/6.1968-658.

[27] Y. Saito, T. Yokoi, H. Yasukochi, K. Soeda, T. Totani, M. Wakita, H. Nagata, Fuel Regression Characteristics of a Novel Axial-Injection End-Burning Hybrid Rocket, J. Propul. Power. 34 (2018) 247–259. https://doi.org/10.2514/1.B36369.

[28] M.A. Hitt, R.A. Frederick, Testing and Modeling of a Porous Axial-Injection, End-Burning Hybrid Motor, J. Propul. Power. 32 (2016) 834–843. https://doi.org/10.2514/1.B35939.

[29] K. Kitagawa, S. Yuasa, Combustion Characteristics of a Swirling LOX Type Hybrid Rocket Engine, J. Jpn. Soc. Aeronaut. Space Sci. 54 (2006) 242–249. https://doi.org/10.2322/jjsass.54.242.

[30] T. Tomizawa, T. Sakurai, Applicability of a LOx vaporization preburner for swirling-flow hybrid rocket engines, 51st AIAA/SAE/ASEE Joint Propulsion Conference. (2015) 1–10. https://doi.org/10.2514/6.2015-4134.

[31] T. Takei, T. Tomizawa, T. Sakurai, Burning characteristics of LOx vaporizatin preburner for A-SOFT HR eingines (in Japanese), in: Japan Society for Aeronautical and Space Sciences (Ed.), Proceedings of the 60th Space Science and Technology Conferenth, {Japan Society for Aeronautical and Space Sciences}, 2016: p. JSASS-2016-4542.

[32] F.C. Johansen, Flow through Pipe Orifices at Low Reynolds Numbers, Proceedings of the Royal Society of London. Series A, Containing Papers of a Mathematical and Physical Character. 110 (1930) 709–737.

[33] A. Tsuji, Y. Saito, L. Kamps, M. Wakita, H. Nagata, Stabilized combustion of circular fuel duct with liquid oxygen, Proc. Combust. Inst. 000 (2020) 1–11. https://doi.org/10.1016/j.proci.2020.07.001.

[34] S. Murakami, Blow-off of a Flame Spreading over Confined Solid Fuels, master thesis (in Japanese), Hokkaido University, 2012.

[35] T. Yokoi, Laminar Flame Spreading Characteristics in a Narrow Fuel Duct, master thesis (in Japanese), Master of Engineering, Hokkaido university, 2017.

[36] Y. Kudo, M. Itakura, Y. Fujita, A. Ito, Flame spread and extinction over thermally thick PMMA in low oxygen concentration flow, Fire Safety Science. (2005) 457–468.

[37] M. Fukada, Stabilized Combustion Characteristics of Micro Port Fuel with N2O, Master thesis (in Japanese), MEn, Hokkaido University, 2021.

[38] S.I. Stoliarov, R.N. Walters, Determination of the heats of gasification of polymers using differential scanning calorimetry, Polym. Degrad. Stab. 93 (2008) 422–427. https://doi.org/10.1016/j.polymdegradstab.2007.11.022.

[39] R.A. Orwoll, Densities, Coefficinets of Thermal Expansion, and Compressibilirities of Aorphous Polymers, in: J.E. Mark (Ed.), Physical Properties of Polymers Handbook, Springer New York, New York, NY, 2007. https://doi.org/10.1007/978-0-387-69002-5.

[40] S.I. Stoliarov, S. Crowley, R.E. Lyon, G.T. Linteris, Prediction of the burning rates of non-charring polymers, Combust. Flame. 156 (2009) 1068–1083. https://doi.org/10.1016/j.combustflame.2008.11.010.

[41] F.W. Dittus, L.M.K. Boelter, Heat transfer in automobile radiators of the tubular type, Int. Commun. Heat Mass Transfer. 12 (1985) 3–22. https://doi.org/10.1016/0735-1933(85)90003-X.

[42] Japan Society of Mechanical Engineering, JSME Data Book : The Thermophysical Properties of Fluids, Japan Society of Mechanical Engineering, 1983.

[43] P.N. Kioni, B. Rogg, K.N.C. Bray, A. Liñán, Flame spread in laminar mixing layers: The triple flame, Combust. Flame. 95 (1993) 276–290. https://doi.org/10.1016/0010-2180(93)90132-m.

[44] R. Azzoni, S. Ratti, S.K. Aggarwal, I.K. Puri, The structure of triple flames stabilized on a slot burner, Combust. Flame. 119 (1999) 23–40. https://doi.org/10.1016/s0010-2180(99)00047-4.

[45] E. Fernández-Tarrazo, A. Liñán, Flame spread over solid fuels in opposite natural convection, Proceedings of the Combustion Institute. 29 (2002) 219–225. https://doi.org/10.1016/s1540-7489(02)80030-x.

[46] S. Li, Q. Yao, C.K. Law, W. Liang, J. Zhuo, Liftoff and blowout of the Emmons flame: Analysis

of the triple flame, Combust. Flame. 215 (2020) 184–192. https://doi.org/10.1016/j.combustflame.2019.12.043.

[47] Y. Otakeyama, T. Yokomori, M. Mizomoto, Stability of CH4-N2/air jet diffusion flame for various burner rim thicknesses, Proc. Combust. Inst. 32 I (2009) 1091–1097. https://doi.org/10.1016/j.proci.2008.05.002.

[48] M. Hirota, T. Yokomori, K. Yasuda, Y. Nagai, M. Mizomoto, G. Masuya, Burning velocity of triple flames with gentle concentration gradient, Proc. Combust. Inst. 31 (2007) 893–899. https://doi.org/10.1016/j.proci.2006.08.068.

[49] A. Liñán, M. Vera, A.L. Sánchez, Ignition, Liftoff, and Extinction of Gaseous Diffusion Flames, Annu. Rev. Fluid Mech. 47 (2015) 293–314. https://doi.org/10.1146/annurev-fluid-010814-014711.

[50] J. Buckmaster, Edge-flames, Prog. Energy Combust. Sci. 28 (2002) 435–475. https://doi.org/10.1016/S0360-1285(02)00008-4.

[51] F. Takahashi, W. John Schmoll, V.R. Katta, Attachment mechanisms of diffusion flames, Symp. Combust. 27 (1998) 675–684. https://doi.org/10.1016/s0082-0784(98)80460-8.

[52] G. Stanford, M. Bonnie J, Computer Program for Calculation of Complex Chemical Equiblium Compositions and Applocations I. Analysis, National Aeronautics and Space Administration, 1994.

[53] S.R. Turns, Appendix B: Fuel Properties, in: S.R. Turns (Ed.), An Introduction to Combustion Concepts and Applications, Third Edition, McGraw-Hill, 2012: pp. 700–703.

[54] CAMEO Chemicals, Methyl Methacrylate, National Oceanic and Atmospheric Administration, 1993. https://cameochemicals.noaa.gov/chemical/7108.

[55] N. Cohen, Revised Group Additivity Values for Enthalpies of Formation (at 298 K) of Carbon–Hydrogen and Carbon–Hydrogen–Oxygen Compounds, J. Phys. Chem. Ref. Data. 25 (1996) 1411. https://doi.org/10.1063/1.555988.

[56] S.W. Grib, M.W. Renfro, Propagation speeds for interacting triple flames, Combust. Flame. 187 (2018) 230–238. https://doi.org/10.1016/j.combustflame.2017.09.018.

[57] N.I. Kim, J.I. Seo, K.C. Oh, H.D. Shin, Lift-off characteristics of triple flame with concentration gradient, Proc. Combust. Inst. 30 (2005) 367–374. https://doi.org/10.1016/j.proci.2004.07.001.

[58] A. Liñán, E. Fernández-Tarrazo, M. Vera, A.L. Sánchez, LIFTED LAMINAR JET DIFFUSION FLAMES, Combust. Sci. Technol. 177 (2005) 933–953. https://doi.org/10.1080/00102200590926932.

[59] S. Bhattacharjee, M.D. King, C. Paolini, Structure of downward spreading flames: a comparison of numerical simulation, experimental results and a simplified parabolic theory, Combust. Theory Model. 8 (2004) 23–39. https://doi.org/10.1088/1364-7830/8/1/002.

[60] Turns, R. Stephen, Appendix D: Binary Diffusion Coefficients and Methodology for their Estimation, in: An Introduction to Combustion Concepts and Applications, McGraw-Hill, NewYork, 2012: pp. 107–109.

[61] B.E. Poling, Poling/pruasnitz, R.C. Reid, J.M. Prausnitz, J.P. O'Connell, T.K. Sherwood, The Properties of Gases and Liquids, McGraw-Hill Education, 2001. https://play.google.com/store/books/details?id=s_NUAAAAMAAJ.

[62] Svehla, R. A., Estimated Viscosities and Thermal Conductivities of Gases at High Temperatures, National Aeronautics and Space Administration, 1962.

[63] M.J. Chiaverini, N. Serin, D.K. Johnson, Y.-C. Lu, K.K. Kuo, G.A. Risha, Regression Rate Behavior of Hybrid Rocket Solid Fuels, J. Propul. Power. 16 (2000) 125–132. https://doi.org/10.2514/2.5541.

[64] M.J. Chiaverini, Review of Solid-Fuel Regression Rate Behavior in Classical and Nonclassical Hybrid Rocket Motors, in: M.J. Chiaverini, K.K. Kuo (Eds.), Fundamentals of Hybrid Rocket Combustion and Propulsion, American Institute of Aeronautics and Astronautics, 2007: pp. 37–126. https://doi.org/10.2514/5.9781600866876.0037.0126.